

Phase Behavior in Rhombohedral NaSiCON Electrolytes and Electrodes

Zeyu Deng,* Gopalakrishnan Sai Gautam, Sanjeev Krishna Kolli, Jean-Noël Chotard, Anthony K. Cheetham, Christian Masquelier, and Pieremanuele Canepa*



Cite This: *Chem. Mater.* 2020, 32, 7908–7920



Read Online

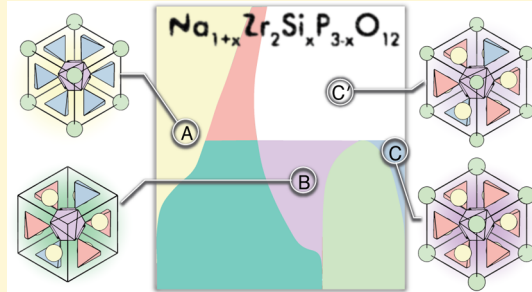
ACCESS |

Metrics & More

Article Recommendations

Supporting Information

ABSTRACT: The replacement of presently used liquid electrolytes by a nonflammable solid electrolytes is an important avenue to create safer batteries. The sodium superionic CONductor (NaSiCON) $\text{Na}_{1+x}\text{Zr}_2\text{Si}_x\text{P}_{3-x}\text{O}_{12}$ ($0 \leq x \leq 3$) that displays high bulk ionic conductivity and good stability toward other NaSiCON-based electrodes is a good solid electrolyte in NaSiCON-based batteries. Despite the sizeable share of research on $\text{Na}_{1+x}\text{Zr}_2\text{Si}_x\text{P}_{3-x}\text{O}_{12}$, the structural and thermodynamic properties of NaSiCON require better understanding for more efficient synthesis and optimization as a solid electrolyte, which often follows chemical intuition. Here, we analyze the thermodynamic properties of the rhombohedral NaSiCON electrolyte by constructing the $\text{Na}_{1+x}\text{Zr}_2\text{Si}_x\text{P}_{3-x}\text{O}_{12}$ phase diagram, based on density functional theory calculations, a cluster expansion framework, and Monte Carlo simulations. Specifically, we build the phase diagram as a function of temperature and composition ($0 \leq x \leq 3$) for the high-temperature rhombohedral structure, which has been also observed in several positive electrode materials, such as $\text{Na}_3\text{Ti}_2(\text{PO}_4)_3$, $\text{Na}_3\text{V}_2(\text{PO}_4)_3$, $\text{Na}_3\text{Cr}_2(\text{PO}_4)_3$, and $\text{Na}_3\text{Fe}_2(\text{PO}_4)_3$. Through the phase diagram, we identify the concentration domains providing the highest Na^+ -ion conductivity and previously unreported phase-separation behavior across three different single-phase regions. Furthermore, we note the similarities in the phase behavior between $\text{Na}_{1+x}\text{Zr}_2\text{Si}_x\text{P}_{3-x}\text{O}_{12}$ and other NaSiCON-based monotransition metal electrodes and discuss the potential competition between thermodynamics and kinetics in experimentally observed phase separation. Our work is an important addition in understanding the thermodynamics of NaSiCON-based materials and in the development of inexpensive Na-ion batteries. From our results, we propose that the addition of SiO_4^{4-} moieties to single-transition metal NaSiCON-phosphate-based electrodes will significantly slow the kinetics toward phase separation.



1. INTRODUCTION

The development of green energy technologies, such as photovoltaics, wind turbines, and rechargeable batteries, is essential in meeting the sustainable needs of a society to limit its fossil fuel usage. Lithium (Li)-ion batteries power the world's mobile devices, and they are increasingly seen in vehicular transportation. When life-cycle analysis is examined in the design of batteries, however, sodium (Na) appears attractive because it can be "harvested" directly from seawater, making Na ~50 times lower in cost than Li.^{1–3} Na-ion batteries also use inexpensive, stainless-steel current collectors.² However, commercial Li-ion batteries and the state-of-the-art Na-ion batteries employ highly flammable organic liquid electrolytes,^{4,5} which pose a tangible safety concern in their widespread deployment.

A pathway to create a battery with a high energy density and safety is to replace the liquid with a nonflammable solid electrolyte,⁶ leading to all-solid-state batteries, which are the object of a sizeable amount of current research.^{7–24} Today, the superionic conductivity of Li^+ and Na^+ ions in solid electrolytes can achieve record values $>10 \text{ mS}\cdot\text{cm}^{-1}$ at room temper-

ature,^{25–27,27} rivaling those of commercial liquid electrolytes (e.g., 1 M LiPF_6 in dimethyl/ethylene carbonates $\sim 10^{-2} \text{ S}\cdot\text{cm}^{-1}$).²⁸ More than 40 years ago, Hong and Goodenough studied the "Natrium Superionic CONductor" (NaSiCON), $\text{Na}_{1+x}\text{Zr}_2\text{Si}_x\text{P}_{3-x}\text{O}_{12}$ ($0 \leq x \leq 3$),^{29,30} which can achieve exceptional bulk ionic Na^+ conductivity ($\sim 15 \text{ mS}\cdot\text{cm}^{-1}$ at 298 K) for $x \sim 2.0\text{--}2.4$.³¹ The NaSiCON structure provides a versatile framework, incorporating both cationic (Na^+ and Zr^{4+}) and anionic (SiO_4^{4-} and PO_4^{3-}) moieties,^{32,33} which enable the number of Na^+ ions to vary between 1 and 4 per formula unit with the corresponding changes in the P/Si ratio and Na^+ -ion conductivity.

Figure 1 depicts the structure of the high-temperature ($>450 \text{ K}$) rhombohedral (space group: $\bar{R}\bar{3}c$) phase of

Received: June 25, 2020

Revised: August 27, 2020

Published: August 27, 2020



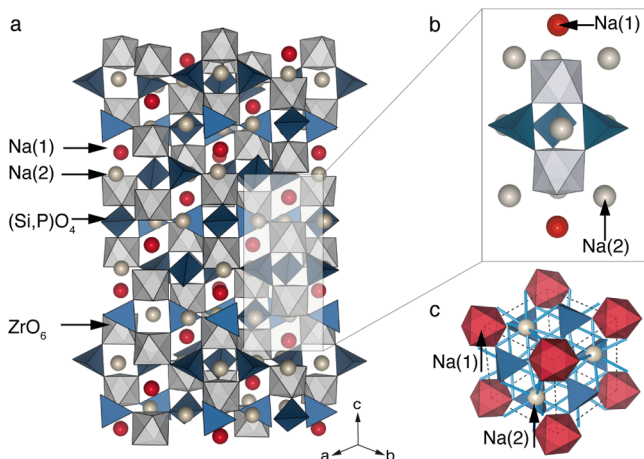


Figure 1. Representation of the rhombohedral $\text{Na}_{1+x}\text{Zr}_2\text{Si}_x\text{P}_{3-x}\text{O}_{12}$ structure. $\text{Na}(1)$ is represented by red antiprisms or red spheres, $\text{Na}(2)$ by silver spheres, $(\text{Si}/\text{P})\text{O}_4$ by blue tetrahedra, and ZrO_6 by gray octahedra. Panel a shows the lantern arrangement, whereby $\text{Na}(1)$ positions are stacked between two ZrO_6 octahedra along the [001] direction. Panel b depicts a zoomed view (of panel a) of the $\text{Na}(1)$ and $\text{Na}(2)$ arrangement within the rhombohedral cell. Panel c shows a view down the c -axis.

$\text{Na}_{1+x}\text{Zr}_2\text{Si}_x\text{P}_{3-x}\text{O}_{12}$ ^{29,30,32,33} where the three blue XO_4 ($\text{X} = \text{P}$ or Si) tetrahedra share corners with two gray ZrO_6 octahedra forming the so-called “lantern units” (panels a and b). There are two distinct, partially occupied (disordered) sodium sites, $\text{Na}(1)$ and $\text{Na}(2)$ (panel b). The superionic behavior in $\text{Na}_{1+x}\text{Zr}_2\text{Si}_x\text{P}_{3-x}\text{O}_{12}$ is driven by a Na-vacancy migration mechanism that relates directly to the occupational disorder of $\text{Na}(1)$ and $\text{Na}(2)$.^{29,34–36} The volume of the polyhedra formed by the $\text{Na}(1)$ site is typically larger than that of $\text{Na}(2)$ and is coordinated by oxygen atoms from ZrO_6 units in an antiprismatic arrangement (Figure 1b,c), while $\text{Na}(2)$ resides in an irregular polyhedral, coordinated to seven neighboring oxygen atoms from the ZrO_6 and XO_4 units. The existence of a third Na site between $\text{Na}(1)$ and $\text{Na}(2)$ has been reported^{33,37} and attributed to a metastable state in the Na^+ migration. At lower temperatures (<450 K) and for $1.8 \leq x \leq 2.2$ for x in $\text{Na}_{1+x}\text{Zr}_2\text{Si}_x\text{P}_{3-x}\text{O}_{12}$, the NaSiCON undergoes a monoclinic distortion (space group: $C2/c$) that is often associated with Na^+ ordering into distinct Na sites and lower Na conductivities.²⁹ Here, we will use the nomenclature rhombohedral and monoclinic NaSiCON to distinguish the two $\text{Na}_{1+x}\text{Zr}_2\text{Si}_x\text{P}_{3-x}\text{O}_{12}$ phases.

There exists an extensive body of prior literature on optimizing the Na-ion conductivity within the NaSiCON electrolyte,^{30,31,33,34,36–40} especially at $x \sim 2$ in $\text{Na}_{1+x}\text{Zr}_2\text{Si}_x\text{P}_{3-x}\text{O}_{12}$. Aliovalent doping has been used to increase the Na-ion conductivity by varying the Na content and disorder in the NaSiCON.^{34,38–40} For example, Miyajima et al.⁴¹ studied the partial substitution of Zr^{4+} by 3+ cations, such as In^{3+} , Yb^{3+} , Er^{3+} , Y^{3+} , Dy^{3+} , Tb^{3+} , and Gd^{3+} in $\text{Na}_{1+x}\text{Zr}_2\text{Si}_x\text{P}_{3-x}\text{O}_{12}$ leading to an increase in the Na content. Although Sc^{3+} has also been used as a common aliovalent dopant on Zr^{4+} ,^{39–41} high Na^+ conductivities ($\sim 3.7 \text{ mS}\cdot\text{cm}^{-1}$) have been achieved by doping with trivalent Al^{3+} , Fe^{3+} , and Y^{3+} and divalent Co^{2+} , Ni^{2+} , and Zn^{2+} species.³⁸ The complete substitution of Zr^{4+} in the NaSiCON by redox-active transition metals,^{36,38–40} for example, Ti, V, Cr, and Fe, in the NaSiCON transforms the solid electrolyte into an

electrode. Notably, NaSiCON-derived electrodes [e.g., $\text{Na}_3\text{Ti}_2(\text{PO}_4)_3$, $\text{Na}_3\text{V}_2(\text{PO}_4)_3$, and $\text{Na}_3\text{Cr}_2(\text{PO}_4)_3$] often show phase-separation behavior upon Na intercalation/extraction.^{34,42,43,43–47}

The phase behavior—phase separation or the existence of solid solutions—has not been fully elucidated in $\text{Na}_{1+x}\text{Zr}_2\text{Si}_x\text{P}_{3-x}\text{O}_{12}$. Specifically, the experimentally observed disorder and fractional occupancies of the Na/vacancy (Va) and Si/P sites in the rhombohedral-NaSiCON structure^{29,30,33} hinder characterization attempts in assigning specific phases (or ordered Na configurations) at different temperatures and Na compositions. In this investigation, we therefore analyze the phase behavior of the NaSiCON electrolyte by constructing the $\text{Na}_{1+x}\text{Zr}_2\text{Si}_x\text{P}_{3-x}\text{O}_{12}$ phase diagram as a function of composition ($0 \leq x \leq 3$) and temperature. We focus on the high-temperature rhombohedral-NaSiCON $\text{Na}_{1+x}\text{Zr}_2\text{Si}_x\text{P}_{3-x}\text{O}_{12}$ structure, which exhibits high Na conductivity and is adopted by several Na-based positive electrodes [e.g., $\text{Na}_3\text{Ti}_2(\text{PO}_4)_3$, $\text{Na}_3\text{V}_2(\text{PO}_4)_3$, $\text{Na}_3\text{Cr}_2(\text{PO}_4)_3$, and $\text{Na}_3\text{Fe}_2(\text{PO}_4)_3$] at high temperature as well. The phase diagram of the rhombohedral $\text{Na}_{1+x}\text{Zr}_2\text{Si}_x\text{P}_{3-x}\text{O}_{12}$ phase is developed by grand canonical Monte Carlo (GCMC) simulations based on a cluster expansion (CE) model,⁴⁸ which is built on density functional theory (DFT)^{49,50} calculations. Importantly, we find specific temperature and Na-concentration domains where the rhombohedral NaSiCON exhibits a biphasic behavior (or phase separation), which is similar to the behavior observed in NaSiCON-based electrodes. Finally, we provide strategies for further optimizing the synthesis of NaSiCON-related materials and improving their ion-transport properties.

2. DETAILS OF MONTE CARLO, CLUSTER EXPANSION, AND DFT CALCULATIONS

To coarse-grain the Gibbs free energy with changes in composition and temperature of the rhombohedral $\text{Na}_{1+x}\text{Zr}_2\text{Si}_x\text{P}_{3-x}\text{O}_{12}$, the Metropolis-Hastings GCMC⁵¹ was performed using a CE Hamiltonian. The CE was parameterized on various Na-vacancy (Va) and Si-P configurations, and the CE fit was obtained using the cluster-assisted statistical mechanics (CASM) code.^{52–55} In performing the GCMC simulations, every Na/Va swap must be coupled to a Si/P swap or vice versa, in order to maintain the charge neutrality of the overall simulation cell. We have enforced the charge neutrality by modifying the GCMC code in the CASM package (<https://github.com/caneparesearch/CASMcode>).^{52–55} GCMC runs were performed on $16 \times 16 \times 16$ supercells of the primitive cell with 172,032 atoms and ranged between 57,344,000 and 573,440,000 steps. The condition of charge neutrality increases substantially the number of GCMC steps required to achieve convergence compared to GCMC simulations without this constraint. GCMC simulations were considered converged when deviations in formation energies reached $\leq 0.5 \text{ meV/f.u.}$

In GCMC, either the chemical potential (μ) or temperature (T) can vary. Because of the charge-neutrality constraint, there is a single independent μ in the NaSiCON system, that is, one unique composition variable (x). As a result of the three ground states in the convex hull at $x = 0$, 2, and 3 (see Section 3.1), μ was scanned in two regions with a fine step size ($\Delta\mu = 0.005 \text{ eV/f.u.}$) in both “forward” and “backward” directions (Section S4 in the Supporting Information, SI). GCMC scans

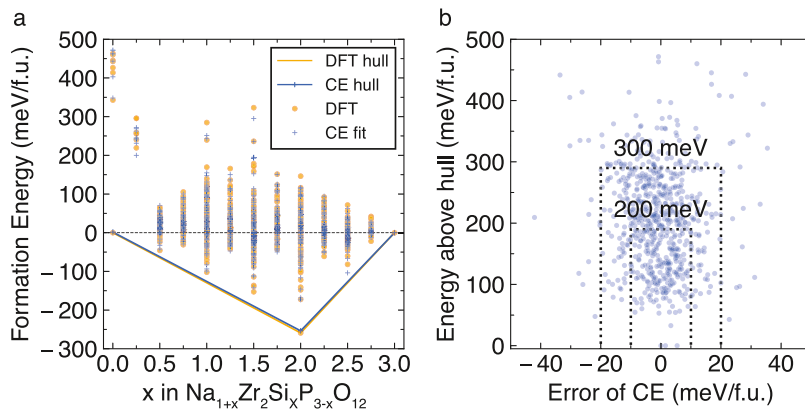


Figure 2. Formation energy of the rhombohedral NaSiCON vs Na/Va (x) and Si/P ($3 - x$) composition (panel a). Orange dots are the formation energies from DFT, while blue crosses depict the energies from the cluster expansion model. The DFT and CE convex hulls are shown by solid orange and blue lines. Panel b plots the error of the CE model with respect to DFT (horizontal axis) vs the energy above the convex hull (vertical axis). The dashed lines in b are confidence windows (of ± 10 and ± 20 meV/f.u.) for the CE model.

were also performed at fixed μ and with varying T from 5 to 1605 K ($\Delta T = 5$ K).

The CE Hamiltonian, based on the approach of Sanchez et al.,⁴⁸ parameterizes the formation energies (E_f in eq 2), as calculated from DFT, of various Na/Va and Si/P configurations, which are mapped onto a fixed $\text{Na}_4\text{Zr}_2\text{Si}_3\text{O}_{12}$ topology. The CE is typically written as a truncated summation of the effective cluster interactions (ECIs) of pair, triplet, quadruplet, and higher-order clusters as

$$E[\vec{\zeta}, \vec{\phi}] = V_0 + V_i \zeta_i + V_{ij} \zeta_i \zeta_j + V_{ia} \zeta_i \phi_a + V_{ab} \phi_a \phi_b + \dots \quad (1)$$

where $E[\vec{\zeta}, \vec{\phi}]$ is the formation energy of a Na/Va and Si/P configuration (i.e., a given structure). The ECI V , and a polynomial function mapping the occupation of the lattice site, with $\zeta_i = 0$ or 1 representing the occupation of Na or Va and $\phi_a = 0$ or 1 that of Si or P.⁵⁰ Each ECI in the sum includes the multiplicity (the cluster symmetry). All symmetrically distinct pairs, triplets, and quadruplets in the rhombohedral cell within a radius of 10, 6, and 5 Å, respectively, are used for constructing the CE model. Note that including larger clusters via increasing the maximum radius (within which clusters are included) results in a dramatic increase in the basis-set size and the complexity of the fitting procedure, without any improvement in the quality of the CE.

Different Na compositions of the rhombohedral NaSiCON were studied by varying the Na content from $\text{Na}_4\text{Zr}_2\text{Si}_3\text{O}_{12}$ to $\text{Na}_1\text{Zr}_2\text{P}_3\text{O}_{12}$. To keep charge neutrality in $\text{Na}_4\text{Zr}_2\text{Si}_3\text{O}_{12}$ upon the “removal” of Na^+ ions (i.e., addition of vacancies), the Si^{4+} ions must also be substituted by P^{5+} ions. Hence, we used the so-called “coupled” CE model⁵⁷ that constrains the concentration of $\text{Si}^{4+}/\text{P}^{5+}$ to Na^+/Va by utilizing a single “point” term (ζ_i) of eq 1. The point term in a CE typically sets μ and the presence of a single μ ensures charge neutrality of the underlying NaSiCON within the CE. Given the large number of clusters available versus the number of DFT-calculated configurations, we used the compressive sensing approach to determine the absolute values of the ECIs by employing $\alpha = 1.5 \times 10^{-5}$ to penalize the L1 norm of the ECIs and minimize overfitting.⁵⁸

Different Na/Va and Si/P configurations were enumerated using the pymatgen package.⁵⁹ The primitive cell of the experimental rhombohedral $\text{Na}_4\text{Zr}_2\text{Si}_3\text{O}_{12}$ structure⁶⁰ (2 f.u.,

with 42 atoms) was used to enumerate the configurations in the possible Na concentration range ($0 \leq x \leq 3$) at a step size, $\Delta x = 0.5$. To keep the number of possible configurations to a computationally tractable level, we used an electrostatic ranking scheme based on the Ewald energy,⁶¹ where classical point charges are assigned to each species (Na = +1, Zr = +4, Si = +4, P = +5, and O = -2). We selected 500 structures at each x with the lowest Ewald energies. We applied a similar enumeration and ranking procedure to obtain Na/Va and Si/P configurations in $2 \times 1 \times 1$ supercells (4 f.u., with 84 atoms, equivalent to $1 \times 2 \times 1$ and $1 \times 1 \times 2$) of the primitive cell with a step size, $\Delta x = 0.25$. The final number of structures considered in our DFT calculations was further reduced by considering only the symmetry inequivalent orderings. In total, we computed 1192 structurally and symmetrically distinct orderings using DFT as implemented in VASP.^{62,63}

The exchange-correlation energy in DFT was approximated by the strongly constrained and appropriately normed (SCAN) semilocal meta-generalized gradient approximation (GGA) functional.⁶⁴ The accuracy of SCAN has been demonstrated on oxides and phosphates,^{65–67} where SCAN has been shown not to overbind O_2 gas, as is typical of GGA functionals.⁶⁸ Wave functions were expanded in terms of a plane-wave basis set, truncated at a kinetic energy cutoff of 520 eV, and combined with projector augmented wave (PAW) potentials to describe the core electrons.⁶⁹ The PAW potentials used were Na_pv 19 Sep 2006 2p⁶3s¹, Zr_sv 04 Jan 2005 4s²4p⁶4d²5s², Si_05 Jan 2001 3s²3p², P_06 Sep 2000 3s²3p³, and O_08 Apr 2002 2s²2p⁴. Total energies were integrated on a $3 \times 3 \times 3$ Monkhorst-Pack grid⁷⁰ for the primitive cells (while the k -point density was maintained for the larger supercells) and converged within 10^{-5} eV/cell, without preserving any symmetry. The atomic forces (and stresses) were converged to within 10^{-2} eV/Å (0.29 GPa).

3. RESULTS

3.1. Energetics of the Na and Si/P Configurations in the Rhombohedral NaSiCON. The formation energy (E_f) of each ordering, computed by DFT, is defined with respect to the lowest energy end-member compositions, $\text{Na}_4\text{Zr}_2\text{Si}_3\text{O}_{12}$ and $\text{Na}_1\text{Zr}_2\text{P}_3\text{O}_{12}$, using eq 2

$$E_f = E[\text{Na}_{1+x}\text{Zr}_2\text{Si}_x\text{P}_{3-x}\text{O}_{12}] + -\frac{x}{3}E[\text{Na}_4\text{Zr}_2\text{Si}_3\text{O}_{12}] - \left(1 - \frac{x}{3}\right)E[\text{Na}_1\text{Zr}_2\text{P}_3\text{O}_{12}] \quad (2)$$

where $E[\text{Na}_{1+x}\text{Zr}_2\text{Si}_x\text{P}_{3-x}\text{O}_{12}]$, $E[\text{Na}_4\text{Zr}_2\text{Si}_3\text{O}_{12}]$, and $E[\text{Na}_1\text{Zr}_2\text{P}_3\text{O}_{12}]$ are the DFT total energies of each Na/Va + Si/P ordering and the two end members. Figure 2 plots the formation energy versus Na composition, which is the phase diagram of the rhombohedral-NaSiCON system at 0 K. The DFT formation energies are shown in orange, whereas the formation energies predicted by the CE model are shown in blue (Figure 2a). The convex envelopes of the structures with the lowest formation energies—the convex hull—as predicted by DFT and CE are depicted by solid orange and solid blue lines, respectively. Importantly, the three lowest energy (or ground state) configurations that lie on both the DFT and CE hulls occur at Na compositions of $x = 0.0$, 2.0 , and 3.0 , in agreement with experimental observations.^{29,71} Thus, there should be a distinct, stable Na/Va (and Si/P) ordering corresponding to the $x = 2.0$ ground-state configuration, apart from the $x = 0.0$ and $x = 3.0$ end members. The structures of the ordered ground-state configurations (the Na/Si/P orderings) that form the convex hull are represented in Figures S3 and S4 of the Supporting Information.

Note that the ground state at $\text{Na}_3\text{Zr}_2\text{Si}_2\text{P}_1\text{O}_{12}$ ($x = 2.0$) distorts away from the rhombohedral symmetry upon DFT structure relaxation, which indicates the tendency for the rhombohedral NaSiCON to transform into the stable low-temperature monoclinic NaSiCON.^{29,37,72,73} It is worth mentioning that any attempt to resolve the Si/P disorder of the rhombohedral primitive cell at $x = 2.0$ reduces the symmetry to a monoclinic arrangement (space group $C2/c$) even prior geometry optimization, that is, ordering the Si/P sites breaks the threefold rotational symmetry of a rhombohedral system. Furthermore, we did not preserve the symmetry in any of our DFT structure relaxations (i.e., impose only a primitive triclinic or $P1$ symmetry). Nevertheless, preserving the symmetry during the DFT calculation leads to a negligible change in the energy of the ground state at $x = 2.0$ (~ 0.274 meV/f.u.). Although the low-temperature monoclinic distortion observed experimentally exhibits the $C2/c$ space group,^{29,37,72,74,75} this structure presents a rotational distortion of the ZrO_6 octahedra in combination with disorder in the Si/P sites, which is not observed in our ground-state structure at $x = 2.0$ (of Figures S3 and S4).

In the case of $x = 0$, the ground-state structure in Figure 2a is ordered and all the Na^+ ions occupy the $\text{Na}(1)$ position (Figures S3 and S4 in the Supporting Information), in agreement with previous experimental reports.^{29,72} The occupation of the $\text{Na}(1)$ sites at low Na concentrations is driven predominantly by the higher electrostatic repulsion between P^{5+} and Na^+ ions compared to Zr^{4+} or Si^{4+} and the closer proximity of $\text{Na}(2)$ sites to P^{5+} than $\text{Na}(1)$. Therefore, any attempt for Na to occupy the $\text{Na}(2)$ sites will increase the instability of these orderings at $x = 0$ and $x = 0.25$, as shown in Figure 2a.

In Figure 2a, most orderings in $2 \times 1 \times 1$ supercells exhibit higher formation energies than configurations within the primitive cell. For example, all the configurations that exhibit $E_f < -50$ meV/f.u. at $x = 0.5$, 1.0 , 1.5 , 2.0 , and 2.5 are orderings within the primitive cell.

3.2. Cluster Expansion Model. Of the 1192 distinct orderings computed by DFT (Figure 2a), only 884 configurations were selected to fit the CE model Hamiltonian. The reduction of our data set is due to the high (and expected) mobility of Na ions in specific starting configurations, which causes Na ions to move from their initial positions during the structure relaxation to final positions that are symmetrically equivalent to other initial Na configurations. We removed selected structures, primarily at $x = 0$ and 0.25 , whose high energies originate from the unfavorable ordering of Na in the structure while making the fitting of the CE extremely challenging. The ECIs obtained via fitting the CE to the DFT formation energies are depicted in Figure 3.

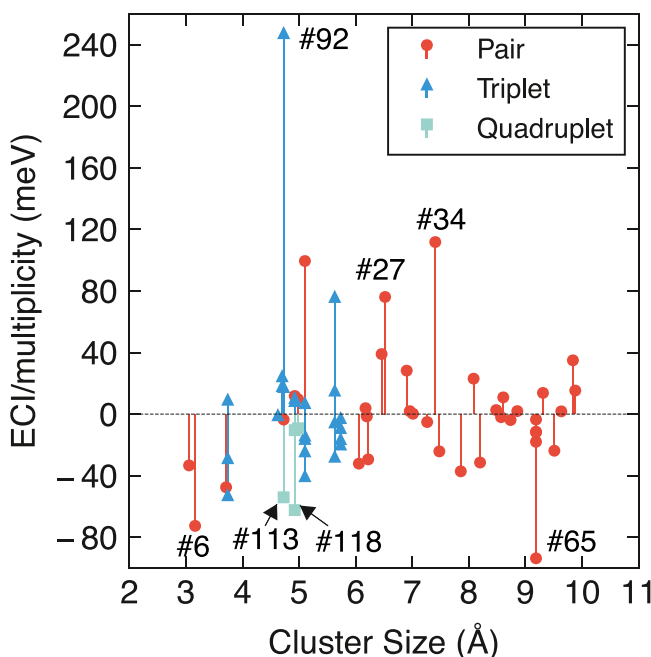


Figure 3. Plot of the 65 ECIs (in meV/multiplicity, vertical axis) vs their size (in Å, horizontal axis). Negative (positive) ECIs in pairs are attractive (repulsive) interactions between Va–Va, P–P, and Va–P. The indexes of specific ECIs are indicated (Table S2 in the Supporting Information).

The ECIs of Figure 3 are obtained by minimizing the root mean square error (RMSE) against the DFT energies of all 884 configurations, which is ~ 11.20 meV/f.u. (~ 0.53 meV/atom), while minimizing the total magnitude of all ECIs to minimize overfitting.⁵⁸ The transferability of the CE is assessed via the leave one-out cross-validation (LOOCV) score, which is ~ 24.9 meV/f.u. (1.18 meV/atom). The 65 clusters with nonzero ECIs are listed in Table S2 of the Supporting Information.

Of the 65 ECIs, 38 ECIs are pair interactions, 22 are triplets, and 4 are quadruplets. In Figure 3, a negative ECI indicates “attractive” interactions between Va for clusters built on Na/Va sites and P for clusters consisting of Si/P sites. Because the NaSiCON structure has both Na/Va and Si/P sites, attractive interactions are also extended to other species with the same occupational variable. Specifically, our CE model uses an identical notation for the occupation of Na/Si ($\sigma = 0$) and Va/P ($\sigma = +1$). Thus, a negative ECI on a Na/Va-Si/P pair translates to an attractive interaction that favors the occupation of Va (on the Na/Va site) and P (on the Si/P site). Similarly, positive ECIs indicate “repulsive” interactions between Va and

P. Because of the specific assignment of $\sigma = 0$ for any Na/Si occupation, only clusters that are fully constituted by Va and/or by P contribute to nonzero ECIs toward the overall energy estimation in our CE model. The dominant pair and triplet terms shown in Figure 3, that is, the highest absolute magnitude ECI, are the repulsive pair cluster #34 (Na/Va-Na/Va of length $\sim 7.40 \text{ \AA}$), the attractive pair cluster #65 (Na/Va-Na/Va, $\sim 9.19 \text{ \AA}$), and the triplet cluster #92 (Na/Va-Na/Va-Na/Va, $\sim 4.72 \text{ \AA}$), respectively. All dominant pair, triplet, and quadruplet interactions within our CE model are listed in Tables S3–S5 of the Supporting Information.

Remarkably, our CE model captures some important physics of the system. For example, the attractive pair #6 (in Figure S1 of the Supporting Information) favors Va located within the cluster formed by one Na(1) and one Na(2) site, separated by a length of $\sim 3.162 \text{ \AA}$ within the primitive rhombohedral cell. However, a larger ($\sim 6.52 \text{ \AA}$) pair cluster #27 (in Figure S1 of the Supporting Information) with Na(1) and Na(2) sites is repulsive, which favors either a Na–Va or a Na–Na occupation within the pair. Thus, the interplay between pair #6 and #27 indicates the competition between short-range versus long-range ordering phenomena in the structure. Furthermore, the most dominant triplet is ECI #92, is repulsive, penalizes the Va–Va–Va occupation, and consists of one Na(1) and two Na(2) sites within the primitive cell (size $< 4.73 \text{ \AA}$), see Table S2 in the Supporting Information. Hence, ECI #92 captures the rather strong short-range interaction between symmetrically distinct Na sites, that is, Na(1) and Na(2) (as elucidated in Section 3.5). Also, the triplet ECI #92 likely acts in conjunction with pairs #27 and #6 [both involving Na(1) and Na(2) sites] to favor a Va–Na–Na configuration on the Na(1)–Na(2)–Na(2) sites, which is the underlying motif of the ground state at $x = 2$ at 0 K (see Figure 2a and Section 3.5). Finally, the quadruplet ECIs #113 and #118 are attractive, span across Na/Va and Si/P sites, and favor occupations of Va–Va–Va–P and Va–Va–P–P, respectively, which likely indicate the electrostatic attraction between Va and P species.

The error in formation energies predicted by the CE expansion model is compared with the energy above the convex hull shown in Figure 2b, with two regions of confidences, ± 10 and $\pm 20 \text{ eV/f.u.}$ (dashed lines). Importantly, the CE reproduces well the DFT formation energies within $\sim 100 \text{ meV/f.u.}$ above the convex hull line. In Figure 2b, points near 0 meV/f.u. on the horizontal axis represent a perfect fit with the DFT data, whereas points beyond $\pm 20 \text{ meV/f.u.}$ can be considered poorly described by the model. Most of the formation energies predicted by the CE model lie within the $\pm 20 \text{ meV/f.u.}$ window, which indicates that the CE can also reproduce the formation energies of several high-energy configurations accurately.

3.3. Temperature–Composition Phase Diagram of the Rhombohedral $\text{Na}_{1+x}\text{Zr}_2\text{Si}_x\text{P}_{3-x}\text{O}_{12}$. Using large simulation cells (172,032 atoms) with GCMC, we can coarse-grain⁷⁶ the grand-canonical potential at any Na(Va)/Si(P) concentration and temperature. The temperature versus Na-composition phase diagram of the rhombohedral $\text{Na}_{1+x}\text{Zr}_2\text{Si}_x\text{P}_{3-x}\text{O}_{12}$, as obtained via GCMC simulations, is shown in Figure 4. The CE method has been proved very accurate in the prediction of Na chemical potentials (and voltages) in electrode materials,^{77,78} which indicates that our methodology is reliable in predicting the useful ranges of μ_{Na} in $\text{Na}_{1+x}\text{Zr}_2\text{Si}_x\text{P}_{3-x}\text{O}_{12}$. The phase boundaries of Figure 4 are

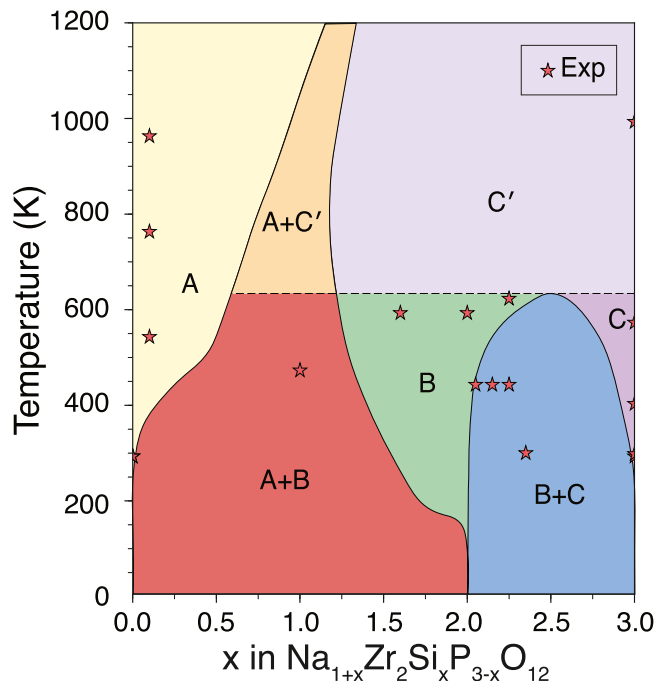


Figure 4. Predicted composition (horizontal axis) vs temperature (vertical axis) phase diagram of rhombohedral $\text{Na}_{1+x}\text{Zr}_2\text{Si}_x\text{P}_{3-x}\text{O}_{12}$ from GCMC simulations. Red stars indicate diffraction studies of rhombohedral NaSiCON reported experimentally.^{33,40,60,79–83}

identified by analyzing the grand-canonical potential energies, the discontinuities of Na concentration (vs μ), and the variation of the heat capacity (vs μ). Numerical hysteresis arising from the GCMC was removed by performing a free-energy integration (see Section S4 and Figure S2 of the Supporting Information).⁷⁶ A representative snapshot of GCMC simulations is provided in Figure S3.

The phase diagram in Figure 4 contains four single-phase (or monophasic) regions, which are labeled A (yellow), B (green), C (dark purple), and C' (light purple), with three two-phase (or biphasic) regions separating the monophasic domains. The biphasic regions are A + B (red dome between $0 < x < 2$, $T < 650 \text{ K}$), A + C' (orange dome, $T > 650 \text{ K}$), and B + C (blue dome between $2 < x < 3$). The monophasic regions can be described as, A: Na-poor domain, similar to the rhombohedral $\text{Na}_1\text{Zr}_2\text{P}_3\text{O}_{12}$; C: Na-rich domain, similar to $\text{Na}_4\text{Zr}_2\text{Si}_3\text{O}_{12}$; B: high-conductivity domain based on the $\text{Na}_3\text{Zr}_2\text{Si}_2\text{P}_1\text{O}_{12}$ configuration, which is the target composition in experimental studies; and C': a high-temperature-disordered domain that encompasses both $\text{Na}_3\text{Zr}_2\text{Si}_2\text{P}_1\text{O}_{12}$ and $\text{Na}_4\text{Zr}_2\text{Si}_3\text{O}_{12}$ regions. Experimentally, the Na/Va and Si/P lattices in the rhombohedral NaSiCON are known to disorder in the composition range $1 < x < 3$ (i.e., excluding the end members) and at high temperatures ($> 473 \text{ K}$),^{9,32,33,33,72,84} in qualitative agreement with our predicted phase diagram.

In the case of the B phase (green domain in Figure 4), at temperatures $< 150 \text{ K}$, phase B is only stable at near $x = 2$, but its stable composition range increases progressively with increasing temperature to a maximum range of $1.25 \leq x \leq 2.5$ at 650 K . The region of stability of the B phase also overlaps with the composition ($1.8 \leq x \leq 2.2$) and temperature ($< 415 \text{ K}$) where the rhombohedral structure transforms into the monoclinic polymorph in experiments.^{29,30,72} Thus, the presence of the B phase may facilitate

the well-known rhombohedral-to-monoclinic transition. At temperatures above 650 K, a high-temperature-disordered phase C' appears, which encompasses both the B and C monophasic regions. The miscibility gap that separates the B and C monophasic regions (blue dome in Figure 4) reaches its critical point at $x = 2.5$ and 650 K. The transition from the high-temperature-disordered C' phase to the miscibility gap (i.e., the B + C two-phase region) represents a first-order phase transition, marked by the dashed black line at 650 K.

The experimental compositions, which are assigned to single-phase regions and determined from X-ray and neutron diffraction measurements, are shown as red stars in Figure 4.^{40,60,72,79–83} Most experimentally observed compositions are found in the single-phase regions of A, B, C, or C' and in good agreement with our calculated phase diagram. Exceptions are reported single-phase structures at $x = 2.0\text{--}2.3$ at 443 K, $x = 0.1$ and 2.35 at 300 K,³³ and $x = 1$ at 473 K.⁴⁰ Although most of the disagreements with experimentally reported single-phase compositions lie at (or near) the predicted phase boundaries, the measured, low-temperature data point at $x = 2.35$, 300 K significantly deviates from our predictions. Notably, the experimental literature, so far, on $\text{Na}_{1+x}\text{Zr}_2\text{Si}_x\text{P}_{3-x}\text{O}_{12}$ has never reported any phase separation in this system.

3.4. Na/Vacancies and Si/P Configurational Effects on the Structural Properties. The DFT-calculated volumes (panel a) and lattice constants a and c (panel b) of the various configurations as a function of the Na composition are shown in Figure 5. Stars represent experimentally reported values of volumes, lattice constants, and c/a ratio,^{29,32,33,60,79–84} whereas dots, squares, and triangles are the DFT-predicted values. The color of each point in Figure 5 is associated with its energy above the convex hull (Figure 2a), with darker blue (lighter white) indicating structures that are near (far away from) the convex hull. The black-dashed lines connect volumes, lattice constants, and c/a ratio of structures forming the convex hull.^{29,32,33,43,85}

Moving from $x = 0$ to $x = 2$ in Figure 5a, the predicted volume increases monotonically with a maximum at $x = 2$ ($\text{Na}_3\text{Zr}_2\text{Si}_2\text{P}_1\text{O}_{12}$), in excellent agreement with experimental reports (distribution of stars). Although DFT calculations do not capture the effect of temperature, the agreement between theory and experiments on lattice volumes can be attributed to the low thermal expansion ($<5\%$, $11.8 \times 10^{-6} \text{ C}^{-1}$) with increasing temperature (over a wide temperature range, i.e., $25 < T < 700^\circ\text{C}$) of the NaSiCON.^{60,79}

In the case of lattice parameters (Figure 5b), we observe that the a parameter increases monotonically with increasing Na content, while the c parameter increases for $0 < x < 2$ and decreases for $x > 2$, in excellent agreement with experimental studies.^{29,33} As the Na content increases in $\text{Na}_{1+x}\text{Zr}_2\text{Si}_x\text{P}_{3-x}\text{O}_{12}$ in the range $0 < x < 2$, the Na^+ ions are displaced from $\text{Na}(1)$ into $\text{Na}(2)$ sites (Figure 6d–f). The reduced occupation of $\text{Na}(1)$ sites facilitates the electrostatic repulsion between ZrO_6 units stacked along the c direction, resulting in an increase in the c parameter.

Importantly, we predict a mild volume contraction ($\sim 1\%$, panel a) for $x > 2$, in agreement with experimental observations that $\text{Na}_4\text{Zr}_2\text{Si}_3\text{O}_{12}$ has a lower volume than $\text{Na}_3\text{Zr}_2\text{Si}_2\text{P}_1\text{O}_{12}$ ($\sim 1\%$ smaller) because of a contraction of the c axis (panel b).⁷⁹ The reduction of the c/a ratio with increasing Na concentration (Figure 5c) captures the typical behavior of the rhombohedral NaSiCON as the Na content is varied (stars in panel c).

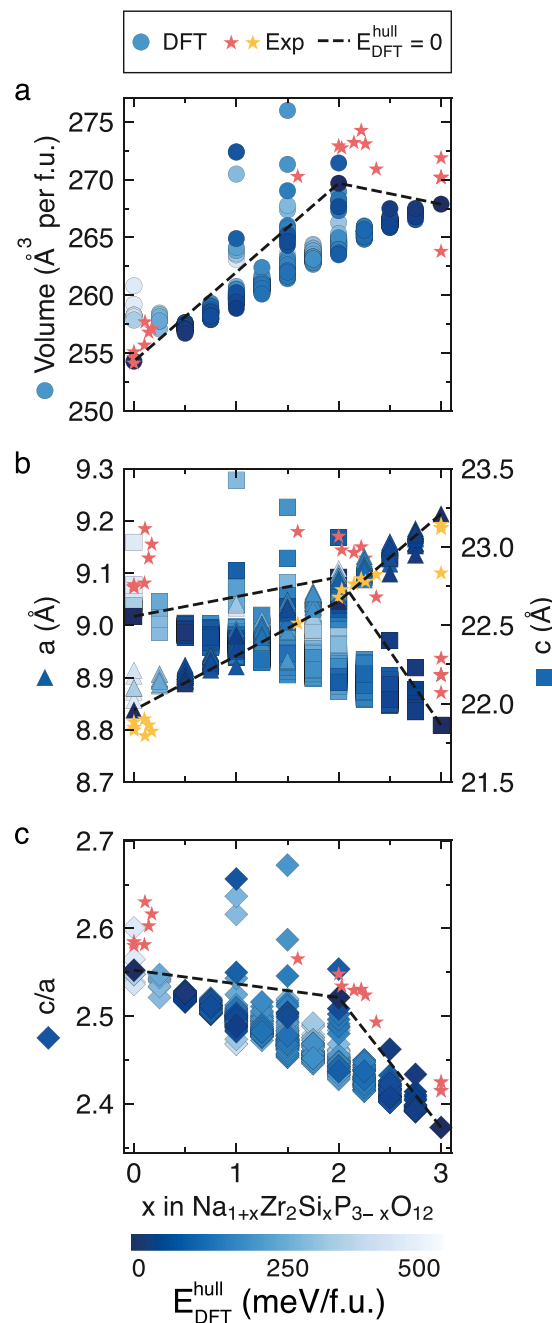


Figure 5. Predicted volumes (vertical axis) in panel a and lattice constants a and c in panel b of rhombohedral NaSiCON vs composition x (horizontal axis). In panel c, the c/a ratio is shown. Each dot, square, or triangle is colored according to its energy above the convex hull. The dashed black line connects ground-state configurations that are on the convex hull at 0 K. Experimentally reported volumes and lattice constants^{29,32,33,60,79–84} at specific concentrations are indicated by stars.

3.5. Thermodynamic Properties and Na Occupations Versus Temperature.

The GCMC data enable the analysis of relevant thermodynamic properties, for example, the Gibbs energy (G , orange dots and lines) and the configurational entropy (S , green dots and lines) functions. These are shown in Figure 6, for 3 distinct temperatures, a 445 K, b 625 K, and c 905 K centered around the $\text{B} + \text{C} \rightarrow \text{C}'$ transition (~ 650 K). Note that the Gibbs energies are referenced to the ground-state end-member configurations, namely, $\text{Na}_1\text{Zr}_2\text{P}_3\text{O}_{12}$ and

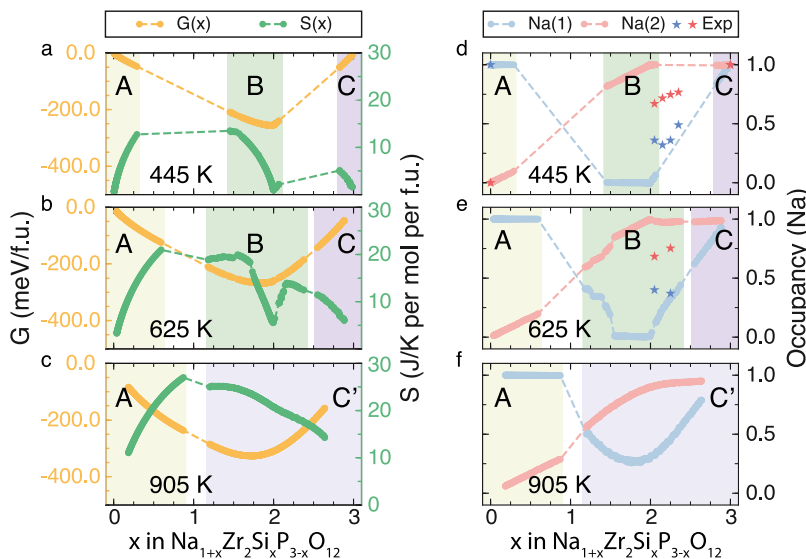


Figure 6. Thermodynamic properties (left panels, a–c) and Na occupancy (right panels, d–f) are shown as a function of Na composition (x , horizontal axis). Gibbs free energy $G(x)$ (orange, left vertical axis) and configurational entropy $S(x)$ (in green, right vertical axis) are shown at specific temperatures 445 K (panel a), 625 K (panel b), and 905 K (panel c), respectively. Panels d, e, and f display the distribution of Na between the two sites, Na(1) (in blue) and Na(2) (in red), at 445, 625, and 905 K, respectively. Experimental data at 443 and 623 K from ref 33 are indicated as blue/red stars for Na(1)/Na(2) sites. Dashed lines indicate regions of phase separation in the phase diagram, while monophasic domains are shown by colored regions (from Figure 4).

$\text{Na}_4\text{Zr}_2\text{Si}_3\text{O}_{12}$. Panels d–f in Figure 6 show the extent of occupation of Na(1) (blue dots and lines) and Na(2) (red dots and lines) by Na^+ versus x at three temperatures, where a fully Na-occupied site (fully empty) has an occupancy of 1.0 (0.0). Notably, the occupation values are obtained as statistical averages from GCMC simulations. Also, the multiplicity of Na(2) is three times that of Na(1), that is, there are three Na(2) sites for every Na(1). Dashed lines in all panels of Figure 6 indicate thermodynamic properties and Na occupancies within biphasic regions.

An increasing temperature typically decreases G , which is consistent with the more negative Gibbs energies at 905 K compared to 445 K, as shown in Figure 6. Although S depends strongly on the temperature, the value of S at a given x depends on the number of accessible configurations at that composition. For example, $S(x = 3) = 0$ at all temperatures because there are no configurational degrees of freedom available at the $\text{Na}_4\text{Zr}_2\text{Si}_3\text{O}_{12}$ composition, that is, no configurations lie above the convex hull at this composition (Figure 2).

Below the $\text{B} + \text{C} \rightarrow \text{C}'$ transition (445 and 625 K), $S(x)$ shows three distinct segments for the three monophasic regions A, B, and C, with three minima of $S(x)$ [and $G(x)$] located at the 0 K ground-state compositions, namely, $x = 0, 2$, and 3. The higher entropy observed for other compositions away from the 0 K ground states is indicative of the higher configurational disorder within the Na/Va and Si/P sublattices. Importantly, the minima in entropy at $x \sim 2$ (within the B monophasic region) at 625 and 445 K correlate with the Na occupancies of the Na(1) and Na(2) sites (Figure 6d–f, see Discussion below). At 905 K (beyond the $\text{B} + \text{C} \rightarrow \text{C}'$ transition), $S(x)$ shows two distinct segments, corresponding to the A and C' monophasic region. The minima in $G(x)$ [and $S(x)$] at $x = 2$ are driven by minima in enthalpy already discussed in Figure 2—a reflection of the stable ordering which enhances the chemical bonding at this composition.

Unraveling the distribution of Na among the Na(1) and Na(2) sites sheds light on the Na-ion transport in NaSiCON phases, which is still not fully understood.³⁷ From Figure 6d–f, we note that for $x = 0$, Na(1) is fully occupied and Na(2) is empty at all temperatures, in agreement with previous reports indicating that $\text{Na}_4\text{Zr}_2\text{P}_3\text{O}_{12}$ is a fully ordered phase, with Na occupying only Na(1).^{71,79} Similarly, at $x = 3$, both Na(1) and Na(2) sites are fully occupied, in agreement with the observations of Hong.²⁹ Interestingly, within the monophasic A region ($x = 0$ to $x \sim 1$) at 905 K, the occupation of Na(2) increases with increasing x , while Na(1) remains fully occupied (Figure 6f).

At higher sodium contents, that is, $x > 2$ (within C'), the occupation of Na(1) increases monotonically toward 1.0 at $x = 3$, while the occupation of Na(2) remains roughly constant (~ 1.0). However, at intermediate Na contents ($x \sim 1.25$ to $x \sim 1.75$), the occupancies of Na(2) and Na(1) show contrasting trends with increasing Na content, that is, as Na(2) sites are occupied by Na, Na(1) sites become unoccupied. This simultaneous occupation and unoccupation of Na(2) and Na(1) sites result in a decrease in configurational entropy (Figure 6c), which eventually reaches a minima at $x \sim 1.75$.

Similar trends in Na(1) and Na(2) occupancies at intermediate Na concentrations can also be observed below the $\text{B} + \text{C} \rightarrow \text{C}'$ transition (panels d and e in Figure 6), in agreement with the trends reported by Boilot and Collin (starts in panels d and e).³³ Notably, the Na(1) sites become empty at Na compositions of $1.5 < x < 2$ within the B domain (at 445 and 625 K), whereas the Na(1) site is never fully empty in C' with the minimum in occupation reaching at $x \sim 1.75$. Also, the Na sites are completely ordered, that is, Na(2) is fully occupied and Na(1) is fully empty, at $x = 2$ within the B phase, whereas complete ordering does not occur at $x = 2$ within the high-temperature C' phase, underlying the key difference between the B and C' monophasic regions. Thus, Na occupying the Na(1) sites is the primary mechanism of

inducing configurational disorder in the NaSiCON structure as the system transitions from ordered B to disordered C', particularly at $x = 2$. Additionally, the complete ordering at $x = 2$ in B corresponds to the minima in entropy observed at 445 and 625 K at $x = 2$ (Figure 6a,b).

4. DISCUSSION

4.1. Reconciling the Phase Behavior in NaSiCON-Based Electrolytes and Electrodes. Understanding the thermodynamic properties of the rhombohedral $\text{Na}_{1+x}\text{Zr}_2\text{Si}_x\text{P}_{3-x}\text{O}_{12}$ and NaSiCON systems in general, is of importance for the development of inexpensive solid electrolytes and electrode materials for novel Na-ion batteries. We have systematically analyzed the phase diagram of rhombohedral $\text{Na}_{1+x}\text{Zr}_2\text{Si}_x\text{P}_{3-x}\text{O}_{12}$ by combining first-principles calculations, the cluster expansion formalism, and Monte Carlo simulations. The computational investigation of the monoclinic phase diagram of $\text{Na}_{1+x}\text{Zr}_2\text{Si}_x\text{P}_{3-x}\text{O}_{12}$ requires knowledge of the end-member structures at $\text{Na} = 1$ and $\text{Na} = 4$, which are only found experimentally in the rhombohedral arrangement. This lack of information curbs the prediction of the monoclinic phase diagram.

The computed phase diagram of Figure 4 reveals the presence of two main regions characterized by biphasic behavior, which are (i) the A + B region that stretches through Na compositions $0 < x < 2$ at low temperatures (below 200 K) and narrows in the composition range with increasing temperature and (ii) the miscibility gap, B + C, in the region $2 < x < 3$ between 0 and ~ 650 K. Our result is in stark contrast with the experimental literature, which indicates a single-phase behavior across the whole region of accessible Na compositions (i.e., $0 \leq x \leq 3$) and temperatures (> 450 K, beyond the region of monoclinic phase stability).^{9,30,32,33,39,40,72} The phase diagram also displays four monophasic regions—A, B, C, and C', with B spanning a noticeably increasing range of Na concentrations with increasing temperature.

Note that Zr off-stoichiometry is often observed in the rhombohedral $\text{Na}_{1+x}\text{Zr}_2\text{Si}_x\text{P}_{3-x}\text{O}_{12}$, with residual ZrO_2 found after high-temperature synthesis and sintering treatments.^{9,31,39,40,86} Our computed phase diagram does not account for Zr off-stoichiometry, and the inclusion of an additional compositional axis would make this study intractable in terms of computational complexity. However, Boilot et al.³² confirmed that Na migration in vacant Zr sites is impeded, indicating that Zr deficiency is less relevant for optimizing the Na conductivity of this material.

Few experimental reports have targeted the structural characterization of rhombohedral $\text{Na}_{1+x}\text{Zr}_2\text{Si}_x\text{P}_{3-x}\text{O}_{12}$ at Na compositions $0 < x < 2$ or $2 < x < 3$.^{29,40} Notably, most of the early characterization work on rhombohedral $\text{Na}_{1+x}\text{Zr}_2\text{Si}_x\text{P}_{3-x}\text{O}_{12}$ used single-crystal samples with $x \geq 2$,^{30,33,72,74,87} which were mostly refined according to the structural model of Hong.²⁹ Although single-crystal X-ray diffraction (XRD) experiments are undoubtedly useful in understanding the structural properties of this material, they may hinder the observation of phase separation in $\text{Na}_{1+x}\text{Zr}_2\text{Si}_x\text{P}_{3-x}\text{O}_{12}$, in particular, across Na-rich and Na-poor composition domains (e.g., A + B and B + C in Figure 4), resulting in the lack of identification of unique mono- or biphasic domains. For this purpose, advanced powder X-ray or neutron diffraction experiments are required because they should identify phase separation and reveal all the crystalline

phases that would eventually coexist in a given sample. Differential scanning calorimetry can also be used to identify the well-documented albeit weak rhombohedral-to-monoclinic phase transition,^{9,40,88} but phase separation has not been observed so far in the rhombohedral phase.

Recent bench³¹ and synchrotron⁴⁰ powder XRD studies demonstrated unequivocally that the low-temperature $\text{Na}_{1+x}\text{Zr}_2\text{Si}_x\text{P}_{3-x}\text{O}_{12}$ compositions behave as a single phase, in contrast to our predictions. For example, Deng et al.⁴⁰ reported a single phase at $\text{Na}_2\text{Zr}_2\text{Si}_1\text{P}_2\text{O}_{12}$ at temperatures of 295 and 473 K, which is in the middle of the A + B two-phase region (Figure 4). The disagreement in terms of phase stabilities at low temperatures (< 500 K) between the theory-predicted thermodynamics (suggesting phase separation) and experimental reports (indicating single-phase behavior) can be also attributed to kinetic factors. For example, at low temperatures (~ 300 K), our predicted phase diagram suggests that $\text{Na}_{3.5}\text{Zr}_2\text{Si}_1\text{P}_2\text{O}_{12}$ (C') will phase-separate into a mixture of $\text{Na}_3\text{Zr}_2\text{Si}_1\text{P}_2\text{O}_{12}$ (B) and $\text{Na}_4\text{Zr}_2\text{Si}_3\text{O}_{12}$ (C). This requires the disordered SiO_4^{4-} and PO_4^{3-} ions in the high-temperature C' phase to be redistributed in order to form the stable B and C phases. The redistribution of the SiO_4^{4-} and PO_4^{3-} , which requires macroscopic diffusion of multivalent Si^{4+} and P^{5+} ions, would involve high activation barriers that are inaccessible at the lower temperatures to ensure full phase separation.⁸⁹ We verified this unsurmountable energetic cost for Si^{4+} and P^{5+} reorganization by computing the migration barrier of P^{5+} in $\text{Na}_{1+x}\text{Zr}_2\text{Si}_x\text{P}_{3-x}\text{O}_{12}$, which results larger than ~ 4.02 eV (Figure S5 in the Supporting Information). However, it remains to be verified experimentally (which we will do in the near future) whether prolonged annealing treatments at intermediate temperatures can promote phase separation in $\text{Na}_{1+x}\text{Zr}_2\text{Si}_x\text{P}_{3-x}\text{O}_{12}$.

Biphasic behavior is typical in NaSiCON-based electrodes. For example, Delmas et al.⁴² detected phase separation of the rhombohedral electrode $\text{Na}_2\text{Ti}_2(\text{PO}_4)_3$ when cooled, leading to the formation of $\text{Na}_3\text{Ti}_2(\text{PO}_4)_3$ and $\text{Na}_1\text{Ti}_2(\text{PO}_4)_3$. For NaSiCON electrodes with a single transition metal [e.g., M = Ti, V, Cr, and Fe in $\text{Na}_x\text{M}_2(\text{PO}_4)_3$], the existence of two-phase domains is also observed in electrochemical experiments, whereby the Na-discharge voltage profile exhibits a flat plateau as Na intercalates in the electrode (see Figure 7).^{42,47}

Notably, mechanisms of phase separation in single-transition-metal NaSiCON electrodes do not involve modifications of the structural framework because phase separation occurs across Na compositions (i.e., the formation of the Na-rich and Na-poor domain) and bond-breaking/reforming involving framework atoms (e.g., Ti, V, Cr, or Fe) is not required, as transition metals do not have to diffuse macroscopically. In other words, the mobile Na^+ and the accompanying electrons can be redistributed swiftly even at low temperatures (~ 300 K) to ensure phase separation. Interestingly, previous studies have claimed that the thermodynamically favorable phase separation was curbed in mixed-transition-metal NaSiCON systems. For example, in $\text{Na}_2\text{ZrCr}(\text{PO}_4)_3$, the phase separation reaction, $2\text{Na}_2\text{ZrCr}(\text{PO}_4)_3 \rightarrow \text{NaZr}_2(\text{PO}_4)_3 + \text{Na}_3\text{Cr}_2(\text{PO}_4)_3$, is inhibited by the slow kinetics of bond-breaking/reforming of Zr–O and Cr–O bonds and the poor macroscopic diffusivity of Zr^{4+} and Cr^{3+} .⁴² Notably, phase separation of $\text{Na}_2\text{ZrCr}(\text{PO}_4)_3$ was not observed even after prolonged annealing treatments at high temperatures. Thus, the thermodynamically favored phase separation in rhombohedral $\text{Na}_{1+x}\text{Zr}_2\text{Si}_x\text{P}_{3-x}\text{O}_{12}$ may also be kinetically

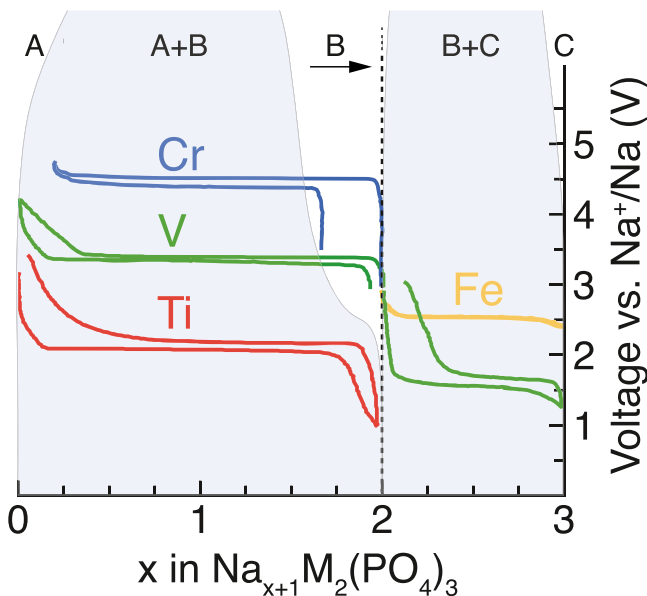


Figure 7. Experimental voltage (vertical axis) charge/discharge curves of $\text{Na}_3\text{Ti}_2(\text{PO}_4)_3$ (in red), $\text{Na}_3\text{V}_2(\text{PO}_4)_3$ (in green), $\text{Na}_3\text{Cr}_2(\text{PO}_4)_3$ (in blue), and $\text{Na}_3\text{Fe}_2(\text{PO}_4)_3$ (in yellow), adapted from refs.,^{43,45,47,85} are superimposed onto the predicted phase diagram of NaSiCON (~295 K) from Figure 4. The dashed line and the arrow indicate the ordering at $x = 2$.

inhibited, similar to the mixed-transition-metal NaSiCON systems.⁴⁴

To illustrate explicitly the similarity between the phase-separation behavior identified in this work in $\text{Na}_{1+x}\text{Zr}_2\text{Si}_x\text{P}_{3-x}\text{O}_{12}$ and as observed in NaSiCON electrodes, we schematically superimpose our computed phase diagram (around 295 K) onto the experimental voltage curves of $\text{Na}_3\text{Ti}_2(\text{PO}_4)_3$, $\text{Na}_3\text{V}_2(\text{PO}_4)_3$, $\text{Na}_3\text{Cr}_2(\text{PO}_4)_3$, and $\text{Na}_3\text{Fe}_2(\text{PO}_4)_3$, as shown in Figure 7.

Similar to $\text{Na}_{1+x}\text{Zr}_2\text{Si}_x\text{P}_{3-x}\text{O}_{12}$, all the electrode materials shown in Figure 7, that is, $\text{Na}_3\text{Ti}_2(\text{PO}_4)_3$, $\text{Na}_3\text{V}_2(\text{PO}_4)_3$, $\text{Na}_3\text{Cr}_2(\text{PO}_4)_3$, and $\text{Na}_3\text{Fe}_2(\text{PO}_4)_3$, crystallize in the rhombohedral structure at $x = 0$ and $x = 3$ and distort into a monoclinic form at $x = 2$.⁷³ Furthermore, the octahedrally coordinated transition metals involved in the redox couples of these NaSiCON electrode materials are not prone to Jahn-Teller distortions,⁹⁰ thus making our comparison with $\text{Na}_{1+x}\text{Zr}_2\text{Si}_x\text{P}_{3-x}\text{O}_{12}$ appropriate.

Figure 7 shows that as Na is inserted/extracted into/from $\text{NaM}_2(\text{PO}_4)_3/\text{Na}_3\text{M}_2(\text{PO}_4)_3$ ($\text{M} = \text{Ti}, \text{V}, \text{Cr}, \text{and Fe}$), the materials always phase-separate for Na concentrations in the range $0 < x < 2$. $\text{Na}_{x+1}\text{V}_2(\text{PO}_4)_3$ also phase-separates between Na concentrations of $2 < x < 3$. Figure 7 identifies that at composition $x = 2$, a stable phase (or structure/configuration) is always found and appears to be common to all NaSiCON-based electrodes, analogous to $\text{Na}_{1+x}\text{Zr}_2\text{Si}_x\text{P}_{3-x}\text{O}_{12}$. Intriguingly, at low temperature and at $x = 2$, all of the Na(2) sites in $\text{Na}_{1+x}\text{Zr}_2\text{Si}_x\text{P}_{3-x}\text{O}_{12}$ are occupied while the Na(1) sites have negligible occupations, similar to trends observed in Figure 6.^{29,33,84} On the basis of our entropy curves shown in Figure 6, we believe that the tendency for Na to order at composition $x = 2$ in $\text{Na}_3\text{V}_2(\text{PO}_4)_3$, $\text{Na}_3\text{Cr}_2(\text{PO}_4)_3$, and $\text{Na}_3\text{Zr}_2\text{Si}_x\text{P}_{3-x}\text{O}_{12}$ is significant and eventually drives the rhombohedral-to-monoclinic (and their superstructures) phase transition at room temperature.^{29,73,91}

In light of these findings, one can formulate the following hypothesis:

- Phase separation appears to be the underlying favorable thermodynamic process in $\text{Na}_{1+x}\text{Zr}_2\text{Si}_x\text{P}_{3-x}\text{O}_{12}$ but is inhibited by the large energy barrier involved in the rearrangement of the SiO_4^{4-} and PO_4^{3-} species.
- Phase separation is fully or partially inhibited, kinetically, whenever cations of the $\text{M}_2(\text{PO}_4)_3$ framework are required to break bonds, migrate, and form new bonds. Analogous to the kinetic impediment to phase separation observed for the solid electrolyte $\text{Na}_{1+x}\text{Zr}_2\text{Si}_x\text{P}_{3-x}\text{O}_{12}$, partial replacement of SiO_4^{4-} and PO_4^{3-} may also kinetically limit any phase separation in monotransition metal electrodes. Other “network formers”, such as SiS_4^{4-} and PS_4^{3-} , found in Li-ion conductors may provide similar effects.⁹²
- In both the solid electrolyte and NaSiCON electrodes, the existence of a stable ordering of Na ions on the Na(2) site at the $x = 2$ composition is a common feature. The stability of the fully occupied Na(2) plus fully empty Na(1) configuration might be electrostatically driven (see Section 4.2) and requires further exploration. As is well-established in the literature, at low temperatures, this peculiar Na configuration seems to promote the phase transition from rhombohedral into monoclinic symmetry, with the rhombohedral \rightarrow monoclinic transformation mechanism needing more work to understand fully.

The validation of these hypotheses and their extension to all NaSiCON-derived electrodes requires further experimental and computational investigations. In particular, the interplay of structural and electronic structure effects needs attention. Importantly, the redistribution of octahedrally coordinated cations in mixed transition-metal NaSiCONs, for example, Ti and Fe in $\text{Na}_x\text{TiFe}(\text{PO}_4)_3$, may be subject to different mechanisms than our predictions for $\text{Na}_{1+x}\text{Zr}_2\text{Si}_x\text{P}_{3-x}\text{O}_{12}$.

4.2. Effects of Na Distributions on the Na Transport in $\text{Na}_{1+x}\text{Zr}_2\text{Si}_x\text{P}_{3-x}\text{O}_{12}$. The bulk ionic conductivity of $\text{Na}_{1+x}\text{Zr}_2\text{Si}_x\text{P}_{3-x}\text{O}_{12}$ is set by the occupations of Na(1) and Na(2) sites,^{31,33,35,37} which enables Na^+ percolation along Na(1)–Na(2)–Na(1) paths. Although Zhang et al.³⁷ investigated the existence of a third Na site, Na(3), located between Na(1) and Na(2), Na(3) is negligibly occupied at high temperatures $200 < T < 800$ °C, hence not relevant to the thermodynamics. Occupancies of Na(1) and Na(2) sites are in turn determined by the distribution of SiO_4^{4-} and PO_4^{3-} groups, in order to maintain “local” charge neutrality within the rhombohedral $\text{Na}_{1+x}\text{Zr}_2\text{Si}_x\text{P}_{3-x}\text{O}_{12}$, an aspect that has been rarely discussed in prior experimental reports. Furthermore, the higher mobility of Na enables Na^+ ions to adopt energy-minimizing configurations, given a Si/P arrangement. Thus, the interplay of local charge neutrality, the short- and long-range cluster interactions among the Na(1) and Na(2) sites, and Na^+ mobility will control the experimentally observed population of Na sites at different Na concentrations.

The GCMC data showed that the occupation of the Na(1) site decreases from $x = 0$ to $x = 2$ and increases monotonically between $x = 2$ and $x = 3$ below the B + C \rightarrow C' transition (see Figure 6). For site Na(2), we observe a constant increase in its occupation in the range $0 < x < 2$, while Na(2) remains fully occupied for $x > 2$. The trends in occupancies of Na(1) and Na(2) sites are in excellent agreement with the experimental

study of Boilot et al.³³ The selective occupation of Na(2) sites at $x \sim 2$ can be attributed to the shorter distance between Na(2) sites and XO_4 tetrahedra, where the increasing occupation of Si in the XO_4 units with increasing x can electrostatically favor Na occupation of Na(2) sites.

It is well-known that a flat energy landscape is beneficial for ion migration,^{93–95} which indicates that the initial and final migration sites should also have comparable energies. In $\text{Na}_{1+x}\text{Zr}_2\text{Si}_x\text{P}_{3-x}\text{O}_{12}$, Na ions migrate between Na(1) and Na(2) sites, and the resultant migration barrier is related to the energy difference between the Na(1) and Na(2) sites when they are occupied by Na. To quantify this aspect, we plot the minimum absolute difference in electrostatic energies (ΔE), based on the classical Ewald summation, between the ground-state (GS) structures and “excited”-state (ES) structures in Figure 8, at $x = 0, 2$, and 3. Note that the GS structures are the

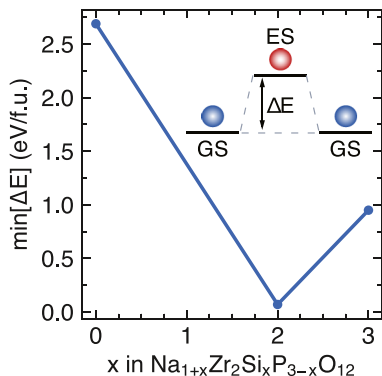


Figure 8. Minimum absolute electrostatic energy difference between the ground-state (GS) and “excited”-state (ES) configurations at Na concentrations of $x = 0, 2$, and 3.

ground-state Na/Si/P configurations at $x = 0$ and 2 (see Figure 6), while at $x = 3$, the GS is the DFT ground state with a Na vacancy. The corresponding ES configurations involve swapping the Na atom/vacancy with an “adjacent” Na(1)/Na(2) site.

In Figure 8, the $\text{min}[\Delta E]$ is significantly high at low (>2.6 eV/f.u. at $x = 0$) and high (>0.9 eV/f.u. at $x = 3$) Na content, signifying high migration barriers for Na transport. In contrast, $\text{min}[\Delta E]$ is low at $x = 2$ (~ 0.14 eV/f.u.), signifying a flat electrostatic energy landscape that may correspond to a low Na migration barrier as well, which is consistent with previous experiments reporting the highest Na^+ conductivity in the range $2 \leq x \leq 2.5$.³³ Although our preliminary analysis does not capture the geometric and bonding effects during Na migration, it should be useful in providing a qualitative guideline of how Na migration barriers (and Na conductivity) vary with Na concentration in the NaSiCON system considered here. However, it remains to be seen how specific configurations of Na/Va and Si/P affect the microscopic migration barriers that govern the overall Na transport. Hence, it is important to extend our model by incorporating migration barriers, as a function of Na content and temperature, which will be the focus of future work.

5. CONCLUSIONS

We investigated the phase stability of the high-temperature $\text{Na}_{1+x}\text{Zr}_2\text{Si}_x\text{P}_{3-x}\text{O}_{12}$ ionic conductor using a multiscale approach based on first-principles calculations, a cluster

expansion framework, and large-size Monte Carlo simulations. We observed excellent agreement with DFT-predicted structural properties, namely, lattice volumes and c and a parameters, with existing measurements. Additionally, we found that the selective occupation of Na(2) sites instead of Na(1) sites drives the stability of the $\text{Na}_3\text{Zr}_2\text{Si}_2\text{P}_1\text{O}_{12}$ ground state, particularly at low temperatures.

The computed phase diagram suggests that $\text{Na}_{1+x}\text{Zr}_2\text{Si}_x\text{P}_{3-x}\text{O}_{12}$ would phase-separate into three distinct single-phase domains at low temperature, in contrast with experimental observations so far. Kinetic limitations, specifically the macroscopic diffusion of Si^{4+} and P^{5+} ions, may inhibit the phase separation into Na + Si-rich and Va + P-rich domains in experiments. We identified similarities in phase behavior between the NaSiCON electrolyte and monotransition-metal NaSiCON electrodes, which typically phase-separate upon Na extraction/insertion. Interestingly, the lack of phase separation observed in mixed-transition-metal NaSiCON electrodes may be attributed to kinetic limitations, similar to the scenario in $\text{Na}_{1+x}\text{Zr}_2\text{Si}_x\text{P}_{3-x}\text{O}_{12}$. Therefore, we speculated that the introduction of SiO_4^{4-} into phosphate-based electrodes can kinetically inhibit phenomena of phase separation.

Based on our phase diagram, we also unveiled the complex interplay between Na site occupancies at different temperatures and electrostatics. With this understanding, we could identify and explain why experimentally only specific compositions offer high Na transport. Our work offers important insights on the role of Na–Va and Si–P configurations on the stability and Na-transport properties of NaSiCON electrolytes and will be an important addition in the development of safe and sustainable Na-ion batteries.

■ ASSOCIATED CONTENT

SI Supporting Information

The Supporting Information is available free of charge at <https://pubs.acs.org/doi/10.1021/acs.chemmater.0c02695>.

Detail of the CE model, detailed description of the Monte Carlo simulation, identification of the phase boundaries, discussion on the free-energy integration, models of ground-state structures, and migration barrier of P^{5+} . All the computational data associated with this study are freely available at the repository <https://github.com/caneparesearch/NaZrSiPO-paper-data> (PDF)

■ AUTHOR INFORMATION

Corresponding Authors

Zeyu Deng – Department of Materials Science and Engineering, National University of Singapore, 117575, Singapore;
 ORCID: [0000-0003-0109-9367](https://orcid.org/0000-0003-0109-9367); Email: msedz@nus.edu.sg

Pieremanuele Canepa – Department of Materials Science and Engineering, National University of Singapore, Singapore;
 ORCID: [0000-0002-5168-9253](https://orcid.org/0000-0002-5168-9253); Email: pcanepa@nus.edu.sg

Authors

Gopalakrishnan Sai Gautam – Department of Materials Engineering, Indian Institute of Science, 560012 Bangalore, India; ORCID: [0000-0002-1303-0976](https://orcid.org/0000-0002-1303-0976)

Sanjeev Krishna Kolli — *Materials Department and Materials Research Laboratory, University of California, Santa Barbara, California 93106, United States; orcid.org/0000-0002-6360-1693*

Jean-Noël Chotard — *Laboratoire de Réactivité et Chimie des Solides, UMR CNRS #7314, Université de Picardie Jules Verne, 80039 Amiens Cedex, France; RS2E, Réseau Français sur le Stockage Electrochimique de l'Energie, FR CNRS #3459, F-80039 Amiens Cedex 1, France; orcid.org/0000-0002-9867-7954*

Anthony K. Cheetham — *Department of Materials Science and Engineering, National University of Singapore, Singapore; Materials Department and Materials Research Laboratory, University of California, Santa Barbara, California 93106, United States; orcid.org/0000-0003-1518-4845*

Christian Masquelier — *Laboratoire de Réactivité et Chimie des Solides, UMR CNRS #7314, Université de Picardie Jules Verne, 80039 Amiens Cedex, France; RS2E, Réseau Français sur le Stockage Electrochimique de l'Energie, FR CNRS #3459, F-80039 Amiens Cedex 1, France; orcid.org/0000-0001-7289-1015*

Complete contact information is available at:
<https://pubs.acs.org/10.1021/acs.chemmater.0c02695>

Author Contributions

P.C. designed and supervised every aspect of the project. Z.D. and P.C. performed the DFT calculations and fitted the cluster expansion model. Z.D. modified the CASM code, performed the Monte Carlo calculations, and carried out the data analysis. Z.D. and P.C. wrote the first draft. Z.D., P.C., G.S.G., and A.K.C. contributed to the initial data analysis of the computed data. All the authors contributed to the discussion and the final version of this manuscript.

Notes

The authors declare no competing financial interest.

ACKNOWLEDGMENTS

P.C., C.M., A.K.C., and J.-N. C. are grateful to the ANR-NRF NRF2019-NRF-ANR073 Na-MASTER. P.C. acknowledges funding from the National Research Foundation under his NRF Fellowship NRFF12-2020-0012. A.K.C., Z.D., and P.C. are grateful to the Green Energy programme under the project code R284-000-185-731. The computational work was performed on resources of the National Supercomputing Centre, Singapore (<https://www.nscc.sg>). P.C. is thankful to Prof. Anton Van der Ven and Prof. Ram Seshadri for hosting Z.D. in their groups at U.C. Santa Barbara.

REFERENCES

- (1) Tarascon, J.-M. Is lithium the new gold? *Nat. Chem.* **2010**, *2*, 510.
- (2) Kim, S.-W.; Seo, D.-H.; Ma, X.; Ceder, G.; Kang, K. Electrode Materials for Rechargeable Sodium-Ion Batteries: Potential Alternatives to Current Lithium-Ion Batteries. *Adv. Energy Mater.* **2012**, *2*, 710–721.
- (3) Clément, R. J.; Bruce, P. G.; Grey, C. P. Review-Manganese-Based P2-Type Transition Metal Oxides as Sodium-Ion Battery Cathode Materials. *J. Electrochem. Soc.* **2015**, *162*, A2589–A2604.
- (4) Goodenough, J. B.; Kim, Y. Challenges for Rechargeable Li Batteries[†]. *Chem. Mater.* **2010**, *22*, 587–603.
- (5) Bachman, J. C.; Muy, S.; Grimaud, A.; Chang, H.-H.; Pour, N.; Lux, S. F.; Paschos, O.; Maglia, F.; Lupart, S.; Lamp, P.; Giordano, L.; Shao-Horn, Y. Inorganic Solid-State Electrolytes for Lithium

Batteries: Mechanisms and Properties Governing Ion Conduction. *Chem. Rev.* **2015**, *116*, 140–162.

(6) Janek, J.; Zeier, W. G. A solid future for battery development. *Nat. Energy* **2016**, *1*, 16141.

(7) Mizuno, F.; Hayashi, A.; Tadanaga, K.; Tatsumisago, M. New, Highly Ion-Conductive Crystals Precipitated from Li₂S-P₂S₅ Glasses. *Adv. Mater.* **2005**, *17*, 918–921.

(8) Kuhn, A.; Duppel, V.; Lotsch, B. V. Tetragonal Li₁₀GeP₂S₁₂ and Li₇GePS₈ - exploring the Li ion dynamics in LGPS Li electrolytes. *Energy Environ. Sci.* **2013**, *6*, 3548.

(9) Lalère, F.; Leriche, J. B.; Courty, M.; Boulineau, S.; Viallet, V.; Masquelier, C.; Seznec, V. An all-solid state NASICON sodium battery operating at 200 °C. *J. Power Sources* **2014**, *247*, 975–980.

(10) Zhu, Y.; He, X.; Mo, Y. Origin of Outstanding Stability in the Lithium Solid Electrolyte Materials: Insights from Thermodynamic Analyses Based on First-Principles Calculations. *ACS Appl. Mater. Interfaces* **2015**, *7*, 23685–23693.

(11) Zhou, W.; Li, Y.; Xin, S.; Goodenough, J. B. Rechargeable Sodium All-Solid-State Battery. *ACS Cent. Sci.* **2017**, *3*, 52–57.

(12) Yu, C.; Ganapathy, S.; van Eck, E. R. H.; Wang, H.; Basak, S.; Li, Z.; Wagemaker, M. Accessing the bottleneck in all-solid state batteries, lithium-ion transport over the solid-electrolyte-electrode interface. *Nat. Commun.* **2017**, *8*, 1086.

(13) El-Shinawi, H.; Regoutz, A.; Payne, D. J.; Cussen, E. J.; Corr, S. A. NASICON LiM₂(PO₄)₃ electrolyte (M = Zr) and electrode (M = Ti) materials for all solid-state Li-ion batteries with high total conductivity and low interfacial resistance. *J. Mater. Chem. A* **2018**, *6*, 5296–5303.

(14) Zhang, Z.; Shao, Y.; Lotsch, B.; Hu, Y.-S.; Li, H.; Janek, J.; Nazar, L. F.; Nan, C.-W.; Maier, J.; Armand, M.; Chen, L. New horizons for inorganic solid state ion conductors. *Energy Environ. Sci.* **2018**, *11*, 1945–1976.

(15) Dawson, J. A.; Canepa, P.; Famprakis, T.; Masquelier, C.; Islam, M. S. Atomic-Scale Influence of Grain Boundaries on Li-Ion Conduction in Solid Electrolytes for All-Solid-State Batteries. *J. Am. Chem. Soc.* **2018**, *140*, 362–368.

(16) Kahle, L.; Marcolongo, A.; Marzari, N. Modeling lithium-ion solid-state electrolytes with a pinball model. *Phys. Rev. Mater.* **2018**, *2*, 065405.

(17) Famprakis, T.; Canepa, P.; Dawson, J. A.; Islam, M. S.; Masquelier, C. Fundamentals of inorganic solid-state electrolytes for batteries. *Nat. Mater.* **2019**, *18*, 1278–1291.

(18) Nolan, A. M.; Liu, Y.; Mo, Y. Solid-State Chemistries Stable with High-Energy Cathodes for Lithium-Ion Batteries. *ACS Energy Lett.* **2019**, *4*, 2444–2451.

(19) Uchida, Y.; Hasegawa, G.; Shima, K.; Inada, M.; Enomoto, N.; Akamatsu, H.; Hayashi, K. Insights into Sodium Ion Transfer at the Na/NASICON Interface Improved by Uniaxial Compression. *ACS Appl. Energy Mater.* **2019**, *2*, 2913–2920.

(20) Schlem, R.; Till, P.; Weiss, M.; Krauskopf, T.; Culver, S. P.; Zeier, W. G. Ionic Conductivity of the NASICON-Related Thiophosphate Na_{1+x}Ti_{2-x}Ga_x(PS₄)₃. *Chem.—Eur. J.* **2019**, *25*, 4143–4148.

(21) Hayashi, A.; Masuzawa, N.; Yubuchi, S.; Tsuji, F.; Hotohama, C.; Sakuda, A.; Tatsumisago, M. A sodium-ion sulfide solid electrolyte with unprecedented conductivity at room temperature. *Nat. Commun.* **2019**, *10*, 5266.

(22) Schwietert, T. K.; Arszelewska, V. A.; Wang, C.; Yu, C.; Vasileiadis, A.; de Klerk, N. J. J.; Hageman, J.; Hupfer, T.; Kerkamm, I.; Xu, Y.; van der Maas, E.; Kelder, E. M.; Ganapathy, S.; Wagemaker, M. Clarifying the relationship between redox activity and electrochemical stability in solid electrolytes. *Nat. Mater.* **2020**, *19*, 428–435.

(23) Kahle, L.; Marcolongo, A.; Marzari, N. High-throughput computational screening for solid-state Li-ion conductors. *Energy Environ. Sci.* **2020**, *13*, 928–948.

(24) Binninger, T.; Marcolongo, A.; Mottet, M.; Weber, V.; Laino, T. Comparison of computational methods for the electrochemical stability window of solid-state electrolyte materials. *J. Mater. Chem. A* **2020**, *8*, 1347–1359.

- (25) Kamaya, N.; Homma, K.; Yamakawa, Y.; Hirayama, M.; Kanno, R.; Yonemura, M.; Kamiyama, T.; Kato, Y.; Hama, S.; Kawamoto, K.; Mitsui, A. A lithium superionic conductor. *Nat. Mater.* **2011**, *10*, 682–686.
- (26) Kato, Y.; Hori, S.; Saito, T.; Suzuki, K.; Hirayama, M.; Mitsui, A.; Yonemura, M.; Iba, H.; Kanno, R. High-power all-solid-state batteries using sulfide superionic conductors. *Nat. Energy* **2016**, *1*, 16030.
- (27) Gao, Y.; Nolan, A. M.; Du, P.; Wu, Y.; Yang, C.; Chen, Q.; Mo, Y.; Bo, S.-H. Classical and Emerging Characterization Techniques for Investigation of Ion Transport Mechanisms in Crystalline Fast Ionic Conductors. *Chem. Rev.* **2020**, *120*, 5954.
- (28) Wang, Y.; Richards, W. D.; Ong, S. P.; Miara, L. J.; Kim, J. C.; Mo, Y.; Ceder, G. Design principles for solid-state lithium superionic conductors. *Nat. Mater.* **2015**, *14*, 1026–1031.
- (29) Hong, H. Y.-P. Crystal structures and crystal chemistry in the system $\text{Na}_{1+x}\text{Zr}_2\text{Si}_x\text{P}_3-\text{xO}_{12}$. *Mater. Res. Bull.* **1976**, *11*, 173–182.
- (30) Goodenough, J. B.; Hong, H. Y.-P.; Kafalas, J. A. Fast Na^+ -ion transport in skeleton structures. *Mater. Res. Bull.* **1976**, *11*, 203–220.
- (31) Ma, Q.; Tsai, C.-L.; Wei, X.-K.; Heggen, M.; Tietz, F.; Irvine, J. T. S. Room temperature demonstration of a sodium superionic conductor with grain conductivity in excess of 0.01 S cm^{-1} and its primary applications in symmetric battery cells. *J. Mater. Chem. A* **2019**, *7*, 7766–7776.
- (32) Boilot, J. P.; Collin, G.; Colombari, P. Crystal structure of the true nasicon: $\text{Na}_3\text{Zr}_2\text{Si}_2\text{PO}_{12}$. *Mater. Res. Bull.* **1987**, *22*, 669–676.
- (33) Boilot, J. P.; Collin, G.; Colombari, P. Relation structure-fast ion conduction in the NASICON solid solution. *J. Solid State Chem.* **1988**, *73*, 160–171.
- (34) Delmas, C.; Viala, J.; Olazcuaga, R.; Leflem, G.; Hagenmuller, P.; Cherkaoui, F.; Brochu, R. Ioni conductivity in Nasicon-type phases $\text{Na}_{1+x}\text{Zr}_2-\text{xLx}(\text{PO}_4)_3$ ($\text{L} = \text{Cr}, \text{In}, \text{Yb}$). *Solid State Ionics* **1981**, *3–4*, 209–214.
- (35) Kohler, H.; Schulz, H. NASICON solid electrolytes part I: The Na^+ -diffusion path and its relation to the structure. *Mater. Res. Bull.* **1985**, *20*, 1461–1471.
- (36) Losilla, E. R.; Aranda, M. A. G.; Bruque, S.; París, M. A.; Sanz, J.; West, A. R. Understanding Na Mobility in NASICON Materials: A Rietveld,23Na and 31P MAS NMR, and Impedance Study. *Chem. Mater.* **1998**, *10*, 665–673.
- (37) Zhang, Z.; Zou, Z.; Kaup, K.; Xiao, R.; Shi, S.; Avdeev, M.; Hu, Y. S.; Wang, D.; He, B.; Li, H.; Huang, X.; Nazar, L. F.; Chen, L. Correlated Migration Invokes Higher Na^+ -Ion Conductivity in NaSICON-Type Solid Electrolytes. *Adv. Energy Mater.* **2019**, *9*, 1902373.
- (38) Jolley, A. G.; Cohn, G.; Hitz, G. T.; Wachsman, E. D. Improving the ionic conductivity of NASICON through aliovalent cation substitution of $\text{Na}_3\text{Zr}_2\text{Si}_2\text{PO}_{12}$. *Ionics* **2015**, *21*, 3031–3038.
- (39) Ma, Q.; Guin, M.; Naqash, S.; Tsai, C.-L.; Tietz, F.; Guillon, O. Scandium-Substituted $\text{Na}_3\text{Zr}_2(\text{SiO}_4)_2(\text{PO}_4)$ Prepared by a Solution-Assisted Solid-State Reaction Method as Sodium-Ion Conductors. *Chem. Mater.* **2016**, *28*, 4821–4828.
- (40) Deng, Y.; Eames, C.; Nguyen, L. H. B.; Pecher, O.; Griffith, K. J.; County, M.; Fleutot, B.; Chotard, J.-N.; Grey, C. P.; Islam, M. S.; Masquelier, C. Crystal Structures, Local Atomic Environments, and Ion Diffusion Mechanisms of Scandium-Substituted Sodium Superionic Conductor (NASICON) Solid Electrolytes. *Chem. Mater.* **2018**, *30*, 2618–2630.
- (41) Miyajima, Y.; Miyoshi, T.; Tamaki, J.; Matsuoka, M.; Yamamoto, Y.; Masquelier, C.; Tabuchi, M.; Saito, Y.; Kageyama, H. Solubility range and ionic conductivity of large trivalent ion doped $\text{Na}_{1+x}\text{M}_x\text{Zr}_2\text{P}_3\text{O}_{11}$ ($\text{M}: \text{In}, \text{Yb}, \text{Er}, \text{Y}, \text{Dy}, \text{Tb}, \text{Gd}$) solid electrolytes. *Solid State Ionics* **1999**, *124*, 201.
- (42) Delmas, C.; Nadiri, A.; Soubeyroux, J. L. The nasicon-type titanium phosphates $\text{Ati}_2(\text{PO}_4)_3$ ($\text{A}=\text{Li}, \text{Na}$) as electrode materials. *Solid State Ionics* **1988**, *28–30*, 419–423.
- (43) Patoux, S.; Rousse, G.; Leriche, J.-B.; Masquelier, C. Structural and Electrochemical Studies of Rhombohedral $\text{Na}_2\text{TiM}(\text{PO}_4)_3$ and $\text{Li}_1.6\text{Na}_0.4\text{TiM}(\text{PO}_4)_3$ ($\text{M} = \text{Fe}, \text{Cr}$) Phosphates. *Chem. Mater.* **2003**, *15*, 2084–2093.
- (44) Masquelier, C.; Croguennec, L. Polyanionic (Phosphates, Silicates, Sulfates) Frameworks as Electrode Materials for Rechargeable Li (or Na) Batteries. *Chem. Rev.* **2013**, *113*, 6552–6591.
- (45) Senguttuvan, P.; Rousse, G.; Arroyo y de Dompablo, M. E.; Vezin, H.; Tarascon, J.-M.; Palacín, M. R. Low-Potential Sodium Insertion in a NASICON-Type Structure through the $\text{Ti}(\text{III})/\text{Ti}(\text{II})$ Redox Couple. *J. Am. Chem. Soc.* **2013**, *135*, 3897–3903.
- (46) Chen, F.; Kovrugin, V. M.; David, R.; Mentré, O.; Fauth, F.; Chotard, J. N.; Masquelier, C. A NASICON-Type Positive Electrode for Na Batteries with High Energy Density: $\text{Na}_4\text{MnV}(\text{PO}_4)_3$. *Small Methods* **2019**, *3*, 1800218.
- (47) Kawai, K.; Zhao, W.; Nishimura, S.-i.; Yamada, A. High-Voltage $\text{Cr}^{4+}/\text{Cr}^{3+}$ Redox Couple in Polyanion Compounds. *ACS Appl. Energy Mater.* **2018**, *1*, 928–931.
- (48) Sanchez, J. M.; Ducastelle, F.; Gratias, D. Generalized cluster description of multicomponent systems. *Phys. A* **1984**, *128*, 334–350.
- (49) Hohenberg, P.; Kohn, W. Inhomogeneous Electron Gas. *Phys. Rev.* **1964**, *136*, B864–B871.
- (50) Kohn, W.; Sham, L. J. Self-Consistent Equations Including Exchange and Correlation Effects. *Phys. Rev.* **1965**, *140*, A1133–A1138.
- (51) Binder, K.; Heermann, D. W. *Monte Carlo Simulation in Statistical Physics: An Introduction*; Binder, K., Heermann, D. W., Eds.; Graduate Texts in Physics; Springer: Berlin, Heidelberg, 2010; pp 5–67.
- (52) Van der Ven, A.; Thomas, J. C.; Xu, Q.; Bhattacharya, J. Linking the electronic structure of solids to their thermodynamic and kinetic properties. *Math. Comput. Simulat.* **2010**, *80*, 1393–1410.
- (53) Puchala, B.; Van der Ven, A. Thermodynamics of the Zr-O system from first-principles calculations. *Phys. Rev. B: Condens. Matter Mater. Phys.* **2013**, *88*, 094108.
- (54) Thomas, J. C.; Van der Ven, A. Finite-temperature properties of strongly anharmonic and mechanically unstable crystal phases from first principles. *Phys. Rev. B: Condens. Matter Mater. Phys.* **2013**, *88*, 214111.
- (55) Developers, C. *Casmcode*: V0.2.1, (visited on 2020/03/24), 2017; <https://zenodo.org/record/546148>.
- (56) Van der Ven, A.; Deng, Z.; Banerjee, S.; Ong, S. P. Rechargeable Alkali-Ion Battery Materials: Theory and Computation. *Chem. Rev.* **2020**, *120*, 6977–7019.
- (57) Zhou, F.; Maxisch, T.; Ceder, G. Configurational Electronic Entropy and the Phase Diagram of Mixed-Valence Oxides: The Case of Li_xFePO_4 . *Phys. Rev. Lett.* **2006**, *97*, 155704.
- (58) Nelson, L. J.; Hart, G. L. W.; Zhou, F.; Ozoliņš, V. Compressive sensing as a paradigm for building physics models. *Phys. Rev. B: Condens. Matter Mater. Phys.* **2013**, *87*, 035125.
- (59) Ong, S. P.; Richards, W. D.; Jain, A.; Hautier, G.; Kocher, M.; Cholia, S.; Gunter, D.; Chevrier, V. L.; Persson, K. A.; Ceder, G. Python Materials Genomics (pymatgen): A robust, open-source python library for materials analysis. *Comput. Mater. Sci.* **2013**, *68*, 314–319.
- (60) Qui, D. T.; Capponi, J. J.; Joubert, J. C.; Shannon, R. D. Crystal structure and ionic conductivity in $\text{Na}_4\text{Zr}_2\text{Si}_3\text{O}_{12}$. *J. Solid State Chem.* **1981**, *39*, 219–229.
- (61) Ewald, P. P. Die Berechnung optischer und elektrostatischer Gitterpotentiale. *Ann. Phys.* **1921**, *369*, 253–287.
- (62) Kresse, G.; Furthmüller, J. Efficient iterative schemes for ab initio total-energy calculations using a plane-wave basis set. *Phys. Rev. B: Condens. Matter Mater. Phys.* **1996**, *54*, 11169–11186.
- (63) Kresse, G.; Furthmüller, J. Efficiency of ab-initio total energy calculations for metals and semiconductors using a plane-wave basis set. *Comput. Mater. Sci.* **1996**, *6*, 15–50.
- (64) Sun, J.; Ruzsinszky, A.; Perdew, J. Strongly Constrained and Appropriately Normed Semilocal Density Functional. *Phys. Rev. Lett.* **2015**, *115*, 036402.

- (65) Sai Gautam, G.; Carter, E. A. Evaluating transition metal oxides within DFT-SCAN and SCAN+U frameworks for solar thermochemical applications. *Phys. Rev. Mater.* **2018**, *2*, 095401.
- (66) Bartel, C. J.; Weimer, A. W.; Lany, S.; Musgrave, C. B.; Holder, A. M. The role of decomposition reactions in assessing first-principles predictions of solid stability. *npj Comput. Mater.* **2019**, *5*, 4.
- (67) Wang, J.; Wang, Y.; Seo, D.-H.; Shi, T.; Chen, S.; Tian, Y.; Kim, H.; Ceder, G. A High-Energy NASICON-Type Cathode Material for Na-Ion Batteries. *Adv. Energy Mater.* **2020**, *10*, 1903968.
- (68) Blöchl, P. E. First-principles calculations of defects in oxygen-deficient silica exposed to hydrogen. *Phys. Rev. B: Condens. Matter Mater. Phys.* **2000**, *62*, 6158–6179.
- (69) Kresse, G.; Joubert, D. From ultrasoft pseudopotentials to the projector augmented-wave method. *Phys. Rev. B: Condens. Matter Mater. Phys.* **1999**, *59*, 1758–1775.
- (70) Monkhorst, H. J.; Pack, J. D. Special points for Brillouin-zone integrations. *Phys. Rev. B: Solid State* **1976**, *13*, 5188–5192.
- (71) Qui, D. T.; Capponi, J. J.; Gondrand, M.; Saib, M.; Joubert, J.; Shannon, R. Thermal expansion of the framework in Nasicon-type structure and its relation to Na^+ mobility. *Solid State Ionics* **1981**, *3–4*, 219–222.
- (72) Boilot, J. P.; Salanié, J. P.; Desplanches, G.; Le Potier, D. Phase Transformations in $\text{Na}_{1+x}\text{Si}_x\text{Zr}_2\text{P}_{3-x}\text{O}_{12}$ Compounds. *Mater. Res. Bull.* **1979**, *14*, 1469.
- (73) Chotard, J.-N.; Rousse, G.; David, R.; Mentré, O.; Courty, M.; Masquelier, C. Discovery of a Sodium-Ordered Form of $\text{Na}_3\text{V}_2-(\text{PO}_4)_3$ below Ambient Temperature. *Chem. Mater.* **2015**, *27*, 5982–5987.
- (74) Kohler, H.; Schulz, H.; Melnikov, O. Composition and conduction mechanism of the NASICON structure X-ray diffraction study on two crystals at different temperatures. *Mater. Res. Bull.* **1983**, *18*, 1143–1152.
- (75) Rudolf, P. R.; Clearfield, A.; Jorgensen, J. D. A time of flight neutron powder rietveld refinement study at elevated temperature on a monoclinic near-stoichiometric NASICON. *J. Solid State Chem.* **1988**, *72*, 100–112.
- (76) van de Walle, A.; Asta, M. Self-driven lattice-model Monte Carlo simulations of alloy thermodynamic properties and phase diagrams. *Modell. Simul. Mater. Sci. Eng.* **2002**, *10*, 521.
- (77) Hinuma, Y.; Meng, Y. S.; Ceder, G. Temperature-concentration phase diagram of P2- Na_xCoO_2 from first-principles calculations. *Phys. Rev. B: Condens. Matter Mater. Phys.* **2008**, *77*, 224111.
- (78) Kaufman, J. L.; Van der Ven, A. Na_xCoO_2 phase stability and hierarchical orderings in the O3/P3 structure family. *Phys. Rev. Mater.* **2019**, *3*, 015402.
- (79) Hazen, R. M.; Finger, L. W.; Agrawal, D. K.; McKinstry, H. A.; Perrotta, A. J. High-temperature crystal chemistry of sodium zirconium phosphate (NZP). *J. Mater. Res.* **1987**, *2*, 329–337.
- (80) Didisheim, J.; Prince, E.; Wuensch, B. Neutron Rietveld analysis of structural changes in NASICON solid solutions $\text{Na}_{1+x}\text{Zr}_2\text{Si}_x\text{P}_3-\text{xO}_{12}$ at elevated temperatures: $x=1.6$ and 2.0 at 320°C. *Solid State Ionics* **1986**, *18–19*, 944–958.
- (81) Kohler, H.; Schulz, H.; Melnikov, O. Structural investigations of NASICON ($\text{Na}_{1+x}\text{Zr}_2\text{Si}_x\text{P}_3-\text{xO}_{12}$; $x=3$) with x-ray diffraction at 298K and 403K. *Mater. Res. Bull.* **1983**, *18*, 589–592.
- (82) Hagman, L.-O.; Kierkegaard, P.; Karvonen, P.; Virtanen, A. I.; Paasivirta, J. The Crystal Structure of $\text{NaM}2\text{IV}(\text{PO}_4)_3$; MeIV = Ge, Ti, Zr. *Acta Chem. Scand.* **1968**, *22*, 1822–1832.
- (83) Kamali, K.; Ravindran, T. R.; Chandra Shekar, N. V.; Pandey, K. K.; Sharma, S. M. Pressure induced phase transformations in $\text{NaZr}_2(\text{PO}_4)_3$ studied by X-ray diffraction and Raman spectroscopy. *J. Solid State Chem.* **2015**, *221*, 285–290.
- (84) Baur, W.; Dygas, J.; Whitmore, D.; Faber, J. Neutron Powder Diffraction Study And Ionic Conductivity Of $\text{Na}_2\text{Zr}_2\text{SiP}_2\text{O}_{12}$ And $\text{Na}_3\text{Zr}_2\text{Si}_2\text{PO}_{12}$. *Solid State Ionics* **1986**, *18–19*, 935.
- (85) Patoux, S. Propriétés structurales et électrochimiques de phosphates d'éléments de transition. Ph.D. Thesis, Université de Picardie Jules Verne, Amiens, 2003.
- (86) Gordon, R.; Miller, G.; McEntire, B.; Beck, E.; Rasmussen, J. Fabrication and characterization of Nasicon electrolytes. *Solid State Ionics* **1981**, *3–4*, 243–248.
- (87) Kohler, H.; Schulz, H. NASICON solid electrolytes Part II - X-ray diffraction experiments on sodium-zirconium-phosphate single crystals at 295K and at 993K. *Mater. Res. Bull.* **1986**, *21*, 23–31.
- (88) Ignaszak, A.; Pasierb, P.; Gajerski, R.; Komornicki, S. Synthesis and properties of Nasicon-type materials. *Thermochim. Acta* **2005**, *426*, 7–14.
- (89) Lalère, F.; Seznec, V.; Courty, M.; David, R.; Chotard, J. N.; Masquelier, C. Improving the energy density of $\text{Na}_3\text{V}_2(\text{PO}_4)_3$ -based positive electrodes through V/Al substitution. *J. Mater. Chem. A* **2015**, *3*, 16198–16205.
- (90) Cox, P. A. *Transition Metal Oxides: An Introduction to Their Electronic Structure and Properties*; Clarendon Press Oxford University Press: Oxford New York, 2010.
- (91) d'Yvoire, F.; Pintard-Scrépel, M.; Bretey, E.; de la Rochère, M. Phase transitions and ionic conduction in 3D skeleton phosphates $\text{A}_3\text{M}_2(\text{PO}_4)_3$: A = Li, Na, Ag, K; M = Cr, Fe. *Solid State Ionics* **1983**, *9–10*, 851–857.
- (92) Kanno, R.; Murayama, M. Lithium Ionic Conductor Thio-LISICON: The $\text{Li}_2\text{S}-\text{GeS}_2-\text{P}_2\text{S}_5$ System. *J. Electrochem. Soc.* **2001**, *148*, A742.
- (93) Rong, Z.; Malik, R.; Canepa, P.; Sai Gautam, G.; Liu, M.; Jain, A.; Persson, K.; Ceder, G. Materials Design Rules for Multivalent Ion Mobility in Intercalation Structures. *Chem. Mater.* **2015**, *27*, 6016–6021.
- (94) He, X.; Zhu, Y.; Mo, Y. Origin of fast ion diffusion in super-ionic conductors. *Nat. Commun.* **2017**, *8*, 15893.
- (95) Canepa, P.; Sai Gautam, G.; Hannah, D. C.; Malik, R.; Liu, M.; Gallagher, K. G.; Persson, K. A.; Ceder, G. Odyssey of Multivalent Cathode Materials: Open Questions and Future Challenges. *Chem. Rev.* **2017**, *117*, 4287–4341.